Propagation of weakly non-linear, narrow-banded waves against strong currents

By Arun Chawla[1] and James T. Kirby[2]

[1]Center for Coastal and Land Margin Research, Oregon Graduate Institute, Portland, OR 97006 USA

[2]Center for Applied Coastal Research, University of Delaware, Newark, DE 19716 USA

(Received ?? and in revised form ??)

Blocking dynamics of gravity water waves have been investigated in a laboratory environment for a range of wave conditions. A non-linear numerical model has been developed to simulate the observed characteristic features of wave blocking. The model is based on a WKB perturbation expansion technique, which is used to study the amplitude evolution of narrow banded spectral waves, but allows for a complex phase to account for wave blocking. The model is one-dimensional and has been width integrated to account for narrowing side walls. The model is susceptible to spurious oscillations that propagate against the waves that are exacerbated in the presence of an opposing current. Numerical filtering techniques are applied to damp out these oscillations. The numerical model does a reasonable job in simulating wave blocking in the smallest amplitude monochromatic wave test cases and also in tests involving wave packets. The model is limited because the location of wave blocking is determined by linear theory, while experimental results indicate that amplitude dispersive effects are very important. The model also blocks the waves at the blocking point of the carrier frequency which is contrary to the observed data, where the wave spectrum is blocked selectively at the blocking points of corresponding wave components. The modeling exercise together with the experimental results throws light on the blocking characteristics of gravity waves, and suggests alternative paths for the development of non-linear wave blocking models.

1. Introduction

Waves propagating against an opposing current can be stopped if the magnitude of the current, in the direction of wave propagation, exceeds the group velocity of the oncoming waves. This phenomenon is known as wave blocking, and the location where the waves are blocked is called the blocking point. Around the blocking point the wave climate transitions rapidly from steepening waves prior to the blocking point (due to the reducing group velocity) to decaying waves beyond the blocking point. This characteristic feature of wave blocking has drawn the interests of oceanographers and coastal engineers alike for their ability to be used as signature patterns of underlying large scale motion (e.g. internal waves) and for the navigational hazards these regions pose. An overview on wave−current interaction studies can be obtained from the comprehensive review works of Peregrine (1976), Jonsson (1990) and Thomas and Klopman (1997).

Dynamic interaction between waves and currents were shown by the works of Longuet-Higgins and Stewart(1960,1961), using the concept of radiation stress, and by Bretherton and Garrett (1969), using the concept of conservation of wave action. Since then dynamics of wave–current interactions have received a lot of attention. Wave blocking phenomena are particularly difficult, since the blocking point forms a caustic leading to singular solutions by ray theory. Using multiple scale analysis and asymptotic expansions Smith (1975), developed uniform solutions for the linear wave field through the blocking region. He showed that in the linear limit the waves are reflected at the blocking point. A similar solution was also found by Peregrine (1976) using stream functions and Fourier transforms. Stiassnie and Dagan (1979) developed a generalized formulation for partial reflection of water waves. The complete reflection test case of Smith (1975) and Peregrine (1976) is a specific example of the more generalized solution. Non-linear effects on wave fields near caustics have been studied by Peregrine and Smith (1979). For the linear solution, Shyu and Phillips (1990) extended the development to include the effects of curved surfaces and capillary effects, so as to investigate the blocking of short waves riding on longer waves. The dynamics of a second reflection point due to the dispersive properties of capillary waves was investigated by Trulsen and Mei (1993) using a boundary layer approximation close to the reflection points. All of the theoretical advances in the dynamics of wave blocking and reflection cited above have been carried out with emphasis on short gravity/capillary waves (mainly for interpreting remote sensing data) and have thus been limited to linear wave approximations (with the exception of Peregrine and Smith (1979)).

Wave blocking, however, is not limited to short gravity/capillary waves. In many coastal environments such as entrances to inlets and estuaries, where wave blocking on ebb tides is observed regularly, the wave climate is considerably energetic. A large number of the waves tend to break and get blocked with minimal reflection. Even in cases with small initial wave amplitude the waves tend to steepen considerably before being blocked due to the combined action of shoaling and shortening. A linear wave approximation is not valid in such environments. Infact, experimental investigations on wave blocking (Chawla and Kirby, 1998,2002) have shown that and amplitude effects can play a major role in the dynamics of wave blocking. Amplitude dispersion effects can considerably alter the location of wave blocking predicted by linear theory, and non-linear processes such as the evolution of side band instabilities can adversely affect the dynamics of the wave field beyond the blocking point. The enhanced nature of side band instabilities in the presence of opposing currents has been reported in the theoretical works of Turpin *et al.* (1983) and Gerber (1987), and have also been confirmed by experimental observations in Lai *et al.* (1989). Chawla and Kirby (2002) have shown that sometimes monochromatic waves can propagate energy beyond the blocking point by down-shifting energy via the growth of side band instabilities to a lower frequency wave. Hence, it is important to include non-linear effects in studying wave blocking. In the experimental studies cited above a varying current was developed by varying the domain, which in itself will also affect the transformation of the wave field. Recently, Suastika *et al.* (2000) have carried out experiments on wave blocking in which the current is varied without varying the domain.

Wave blocking processes have been modeled by Chen *et al.* (1998) using a sophisticated non-linear Boussinesq model, that is not limited by ray theory approximations. Boussinesq models however are limited by their weak dispersive properties in intermediate to deep water environments ($kh < 1.5$), where a lot of the wave blocking occurs. Since the dispersion relation is crucial to predicting the location of wave blocking, a non-linear numerical model with strong dispersive properties is desired that can simulate wave blocking. A boundary integral model has been used by Moreira and Peregrine (2001) and Moreira (2001) to study the phenomenon of wave blocking in deep water.

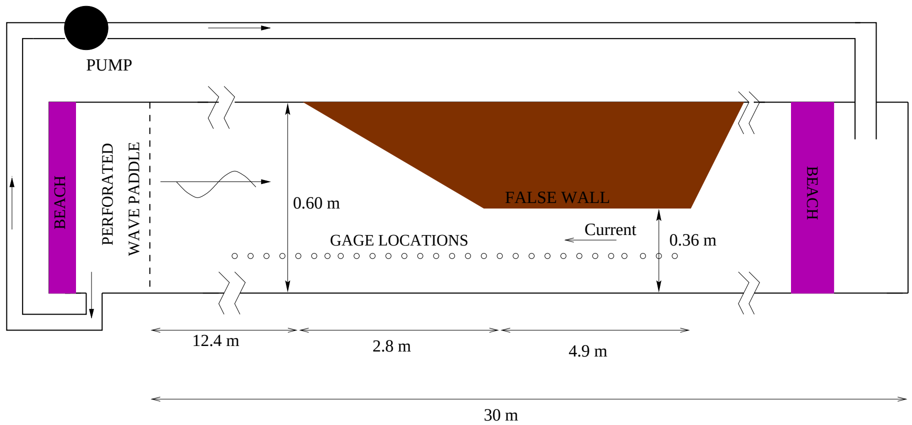

FIGURE 1. Schematic plan view of the experimental setup

Their model has shown considerable promise with being able to simulate both partial wave blocking and blocking of individual waves in a wave group.

Considerable success has been achieved in studying the non-linear evolution of monochromatic waves in deep water by developing a cubic Schrödinger equation for the slowly varying amplitude envelope (Zakharov 1968, Davey 1972, Hasimoto and Ono 1972, Yuen and Lake 1975). Similar types of evolution equations have also been developed for waves in the presence of a slowly varying current (Turpin *et al.* 1983, Gerber 1987). Encouraged by these results, and with the aim to better understand the non-linear aspects of wave blocking, in this paper we seek to develop a similar non-linear model for the slowly varying amplitude envelope that includes the effects of wave blocking. The experimental tests which have served as the basis for choosing the type of model desired have been described in section 2, while the model itself is described in sections 3 and 4. The comparisons between the model and data is given in section 5.

2. Experimental tests

A series of experimental studies on wave blocking by strong opposing currents were conducted in the Center for Applied Coastal Research at the University of Delaware and have been reported in great detail in Chawla and Kirby (1999). The experiments were carried out in a 30 m long flume. A schematic plan view of the experimental setup is shown in Figure 1. Opposing currents were generated with the help of a recirculating pump, and the current was increased in the middle by narrowing the width of the flume with the help of a false wall. The width of the narrow channel is 0.36 m, while the width of the flume is 0.6 m. The experiments were conducted in 0.5 m water depth. Velocity measurements were made with a SONTEK acoustic doppler velocimeter (ADV). Water surface elevation measurements were made with capacitance wave gages. The experiments were designed such that wave blocking occurred around the entrance of the narrow channel.

The origin is placed at the entrance of the narrow channel with the x coordinate axis pointing down the length of the flume and positive in the direction of the waves. Thus, the opposing current starts increasing at $x = -2.8$ m, and reaches its maximum value at $x = 0$ m. The narrow channel extends from $x = 0$ m to $x = 4.9$ m. No measurements were made beyond this point. Due to symmetry the side wall of the flume becomes the center line of the inlet. The y coordinate axis points positive toward the false wall with

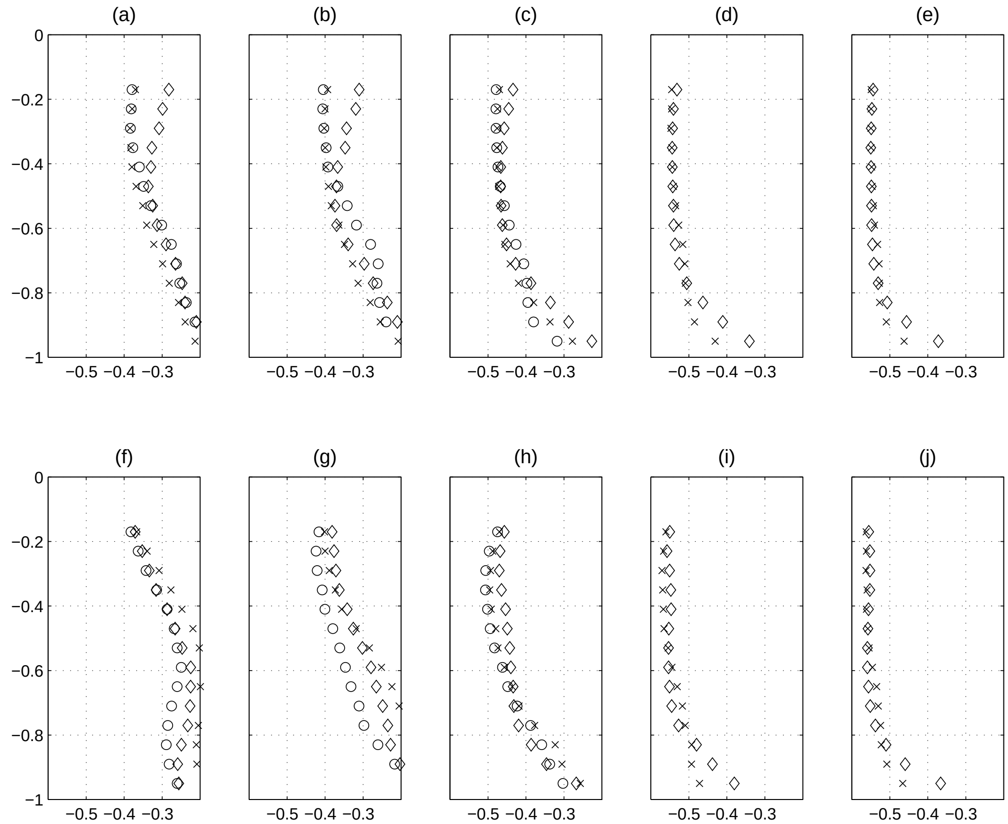

FIGURE 2. Mean current velocity profiles at different locations in the channel. Horizontal axis is the mean current in m/s, while the vertical axis is the normalized vertical position with 0 being the undisturbed free surface and -1 the bottom. **(a)** $\rightarrow$ Velocity profiles at $x = -4.2m$ and $y = 0.15m$ ('×'), $y = 0.30m$ ('∘'), $y = 0.45m$ ('⋄'); **(b)** $\rightarrow$ Velocity profiles at $x = -2.7m$ and $y = 0.15m$ ('×'), $y = 0.30m$ ('∘'), $y = 0.45m$ ('⋄'); **(c)** $\rightarrow$ Velocity profiles at $x = -1.2m$ and $y = 0.13m$ ('×'), $y = 0.23m$ ('∘'), $y = 0.33m$ ('⋄'); **(d)** $\rightarrow$ Velocity profiles at $x = -0.2m$ and $y = 0.13m$ ('×'), $y = 0.25m$ ('⋄'); **(e)** $\rightarrow$ Velocity profiles at $x = 0.8m$ and $y = 0.13m$ ('×'), $y = 0.25m$ ('⋄'); **(f)** $-$ **(j)** $\rightarrow$ same as **(a)** $-$ **(e)** but in the presence of a breaking monochromatic wave

$y = 0$ at the centerline (right wall of the tank). The z coordinate axis points positive upward with $z = 0$ at the still water level.

One of the primary assumptions of this study is that the underlying current is uniform across the cross section of the channel. To test the validity of this assumption the mean velocity profile was computed at different positions in the channel using a SONTEK ADV. Due to structural limitations of the experimental setup, velocity profiles close to the surface could not be computed. The velocity profiles at different cross sections, both in the presence and absence of an opposing monochromatic breaking wave are shown in Figure 2. There is considerable variation in the mean velocity, both in the vertical and across the channel at $x = -4.2m$ and $x = -2.7m$. However, wave blocking occurs close to the mouth of the narrow channel ($x = 0$ m), where the cross channel variation is very insignificant and variation in the vertical is limited to the bottom of the channel. Hence, a uniform current across the channel cross section is a fairly valid assumption.

The experimental tests were divided into three major groups - monochromatic wave tests, random wave tests, and narrow banded spectral tests (wave groups and wave packets). In this paper, we shall concentrate on the monochromatic and narrow banded spectral tests. The breaking characteristics of monochromatic and random wave fields as they propagate through regions of strong opposing currents have been discussed in Chawla and Kirby (2002).

2.1. *Monochromatic wave tests*

A set of 18 different monochromatic wave tests were conducted. In the tests three different wave periods of 1.2s, 1.3s and 1.4s were used. The wave heights were varied to cover a range of conditions, from wave reflection with minimal dissipation to current limited wave breaking being the dominant process. These tests were first described in Chawla and Kirby (1998) and later covered in great detail in Chawla and Kirby (2002). For the purposes of this manuscript, some of the conclusions from Chawla and Kirby (2002) shall be repeated here. The reader is referred to that manuscript for greater detail.

Wave blocking is observed in the shorter amplitude test cases. The shoaling effect decreases with increasing wave height due to current-limited wave breaking (see Figure 8 in Chawla and Kirby (2002)). Amplitude dispersion effects play an important role in determining the onset of wave blocking, with larger amplitude waves being blocked later. For the very large amplitude tests, no wave blocking occurs because of the transfer of energy to lower frequency components which do not meet the blocking condition (see Figure 11 in Chawla and Kirby (2002)). The mechanism for this transfer of energy is through the growth of side band instabilities, which is a non-linear process and is observed only in steep deep water waves.

For the smallest amplitude test cases (with no wave breaking), wave reflection from the blocking point was observed. Reflection at the blocking point involves the transfer of energy between two waves which are both apparently propagating upstream against the current, but where group velocity in the reflected wave is less than current speed, causing it's energy to be swept downstream. The reflected waves get shorter with distance away from the blocking point (Trulsen and Mei 1993, Shyu and Phillips 1990). These short waves were visually observed in the experiments just after the first wave crests were blocked. No wave reflection was observed for the larger wave amplitudes because of energy dissipation due to wave breaking. To observe the dynamics of wave reflection, a second set of monochromatic wave tests were conducted in which the wave amplitude was slowly varied to cover a range of blocking conditions from reflection with not much dissipation to complete dissipation with no discernible reflection (see Table 1 for test particulars). Gages were placed very close to each other around the blocking region to capture the spatial variation of the amplitude. Since these results have not been covered in the earlier manuscripts, they shall be covered in some detail here.

Figure 3 shows the spatial variation of amplitude for the different test conditions. The spatial variation of amplitude shows a distinct transition as the initial wave amplitude increases. Linear theory predicts the spatial variation of amplitude around the blocking region to be described by an Airy function (Smith 1975), given by

$$a = b_0 Ai(\alpha^{2/3}(x - x_{st})) \tag{2.1}$$

where, a is the wave amplitude, b_0 is a function related to the initial incident wave amplitude (see Trulsen and Mei (1993) for details), x_{st} is the location of the blocking point based on linear theory, and

$$\alpha = \sqrt{\frac{2\frac{dU}{dx}k\sigma}{U^2}}|_{x=x_{st}}.$$

TABLE 1. Parameters for reflected monochromatic wave tests (determined at $x = -4.6$ m), where H is the wave height, h is the water depth and k is the wave number determined from the doppler-shifted linear dispersion relation.

Test No.	T (sec)	H (m)	$kH/2$	kh
1	1.2	0.0125	0.029	2.35
2	1.2	0.0129	0.030	2.35
3	1.2	0.0136	0.032	2.35
4	1.2	0.0145	0.034	2.35
5	1.2	0.0159	0.037	2.35

The Airy function distribution is shown by the solid line in Figure 3. Since, the aim here was to see how well the amplitude distribution resembles an Airy function, a detailed modeling of the amplitude distribution was not attempted here. Instead, b_0 was taken to be constant and scaled such that the Airy function and data matched at the smaller peak of the amplitude distribution. From the figure we see that the Airy function describes the amplitude distribution fairly well in Test 1, except at the larger peak, which is probably due to non-linear effects. The mismatch at the minima of the envelopes is enhanced by fluctuations of the water surface owing to fluid turbulence, which can form the dominant part of the water surface signature when wave height is small. With increasing initial amplitude, the amplitude distribution deviates from the Airy function. The effect of non-linear processes can be seen clearly in the shifting of the blocking point with increasing amplitude. The decay beyond the blocking point is also stronger, probably due to the advent of wave breaking, and the signs of wave reflection (the nodal/anti-nodal distribution of wave amplitude) also disappears.

2.2. *Narrow banded spectral tests*

Two sets of experiments were conducted. The first set consisted of a series of tests on wave groups generated by a bichromatic spectrum, while the second set was a series of tests on wave packets generated by a Gaussian shaped spectrum. The aim was to study the evolution of the wave field through the blocking region, and also if the moving blocking point, due to the temporally varying amplitude envelope of a narrow banded spectrum, acts as a generating mechanism for long waves downstream of the blocking region in a way similar to the moving breaker line in nearshore regions.

2.2.1. *Wave groups*

Wave groups were constructed by superposing two monochromatic waves having the same amplitude but slightly different frequencies. The difference between the frequencies determining the number of waves in a group. Three different sets of wave groups were used. Each set consisted of 4 different energy levels, making a total of 12 tests. The test particulars are given in Table 2, where the tests with similar frequencies have been grouped together. 36 gage measurements were made for each test between $x = -4.6$ m and $x = 4.61$ m.

From frequency spectra plots (figure not shown) it was found that even though a bichromatic signal was sent to the wavemaker, in most of the test cases the waves do not remain bichromatic by the time they reach the first gage. For the larger wave amplitude tests, wave energy is transferred to the side bands. Also when the frequency of one

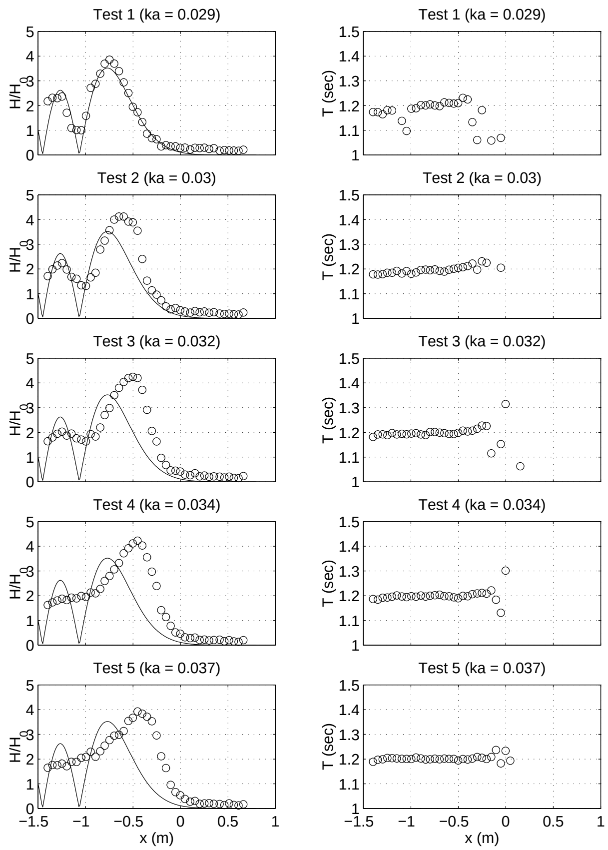

FIGURE 3. Wave height and period distribution for the reflected monochromatic wave tests. Solid line represents an Airy function. Narrow part of the channel begins at $x = 0$

of the design wave components is close to 1 hz, the growth of an anomalous third wave component is observed. This anomalous wave component does not have significant energy in Tests 5,6,11 and 12, where the design frequencies are further away from 1 Hz. The cleanest wave groups at the first gage were observed for Test 6. Thus, only results from this test shall be presented here.

The evolution of the wave groups through the blocking region for Test 6 is shown in Figures 4 and 5. The figures show the time series at 12 different locations in the channel. The corresponding spectral plots are shown in Figure 6. As the waves propagate into stronger currents, the higher frequency wave component being shorter has the higher shoaling coefficient. As a result, in the initial stages there is greater energy in the higher frequency component. However, with increasing opposing current, the steeper higher frequency component starts breaking and losing energy till it's blocking criterion is met. Subsequently, beyond $x = -0.4$ m, the waves are transformed from being groupy to being monochromatic. The lower frequency component continues to lose energy due to the combined action of wave breaking and growth of side band instabilities. At $x = 1.2$ m, the wave field becomes groupy again due to equal energy levels in the primary lower frequency component and its side bands. Beyond that point, the primary wave component is also blocked. It should also be noted that prior to being transformed from a groupy time series to a monochromatic time series, the wave groups transform from being symmetric (at $x = -4.6$ m) to asymmetric (at $x = -1.393$ m and $x = -0.793$ m). This

TABLE 2. Parameters for wave group tests determined at $x = -4.6$ m

Test No.	T_1 (s)	T_2 (s)	H_s (m)	Sampling freq (hz)
1	1.06	1.2	0.028	88.889
2	1.06	1.2	0.054	88.889
7	1.06	1.2	0.068	88.889
8	1.06	1.2	0.098	88.889
3	1.01	1.3	0.028	87.912
4	1.01	1.3	0.054	87.912
9	1.01	1.3	0.068	87.912
10	1.01	1.3	0.083	87.912
5	1.15	1.3	0.025	82.051
6	1.15	1.3	0.053	82.051
11	1.15	1.3	0.074	82.051
12	1.15	1.3	0.089	82.051

is probably due to the wave amplitudes of the individual wave components transforming differently under the opposing current. The experiment shows that the characteristics of wave groups, under blocking conditions are determined by the properties of the individual monochromatic wave components. Similar results were also observed by Chen *et al.* (1998) (for intermediate to shallow water depths) and Moreira (2001) (for deep water waves) in their numerical simulations. No significant long wave energy was observed downstream of the blocking region, and the only effects of the beats in the wave groups seems to be the enhanced wave breaking at the crests of the beats.

2.2.2. *Wave Packets*

Wave packets have been generated with the help of Gaussian shaped frequency spectra. For our experiments 12 design test conditions were generated. As in the case of the wave group tests, these tests have been divided into 3 sets. Each set consisting of 4 different test conditions with varying energy content. The equation for the design spectra was given by

$$S(f) = \frac{\gamma}{\sqrt{2\pi}\alpha}\exp\Big[-0.5\frac{(f-f_p)^2}{\alpha^2}\Big] \tag{2.2}$$

where, f_p is the peak frequency, and γ and α are coefficients determining the energy content and width of the spectrum. The larger the value of α, the lesser the number of individual wave components in the packet. The test particulars for the wave packet tests are given in Table 3. H_{max} is the maximum wave height in the wave packet. T_p is the peak period and α is the parameter used in (2.2).

Similar to the wave group tests, Test 6 consists of a relatively clean packet and the evolution of this packet in space is shown in Figure 7. The amplitude envelopes of the wave packets have been computed using continuous wavelet transforms (CWT). CWT techniques resolve a time series in both frequency and temporal space and are useful for analyzing non-stationary signals. Here they have been employed to determine the amplitude variations at the peak period T_p only. Analysis was performed using the Morlet wavelet. Figure 8 shows the spatial evolution of the amplitude envelope computed by CWT. In the region close to the blocking point, the amplitude envelope shows the presence of two wave packets. Since the temporal separation between the two wave packets

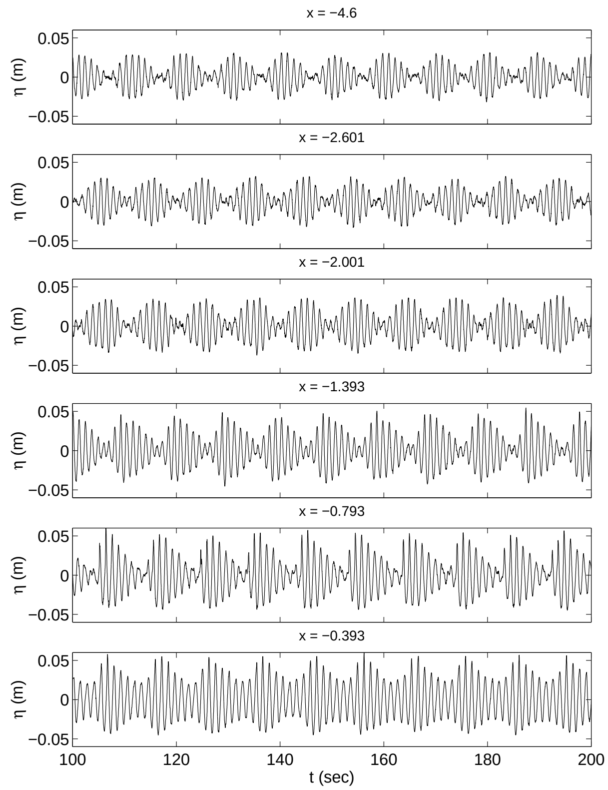

FIGURE 4. Time series of the wave groups at six different locations in the channel (Test 6)

TABLE 3. Parameters for wave packet tests determined at $x = -4.6$ m

Test No.	T_p (s)	H_{max} (m)	α
1	1.125	0.0175	0.08
2	1.125	0.035	0.08
7	1.125	0.07	0.08
8	1.125	0.094	0.08
3	1.137	0.013	0.15
4	1.137	0.02	0.15
9	1.137	0.031	0.15
10	1.137	0.05	0.15
5	1.219	0.017	0.08
6	1.219	0.032	0.08
11	1.219	0.054	0.08
12	1.219	0.084	0.08

increases further behind the blocking point, the second wave packet must represent waves reflected from the blocking point. The energy in the smaller wave packets also decreases for gages located further from the blocking region, which is expected from the reflected waves. At $x = 0$, which is very close to the blocking point the reflected and incident wave

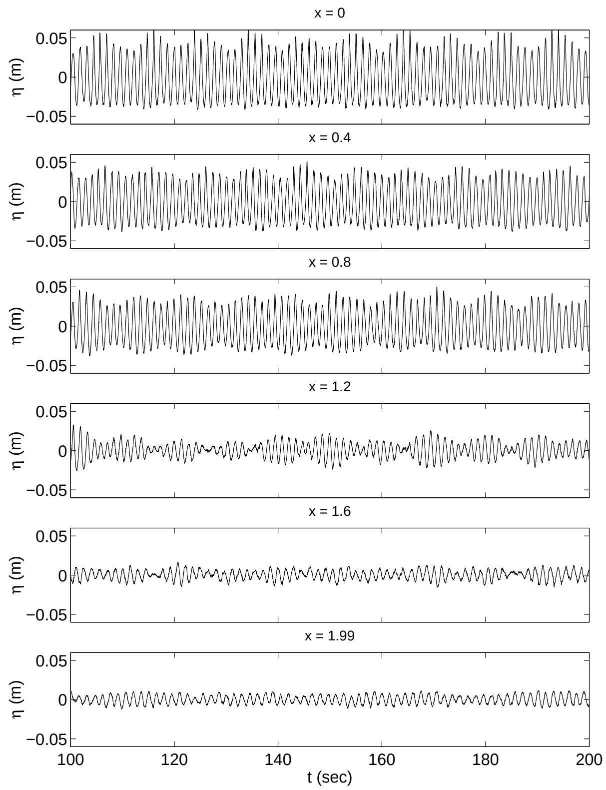

FIGURE 5. Time series of the wave groups at six different locations in the channel (Test 6)

packets are indistinguishable, and we have a more or less symmetric amplitude envelope. The spectral plots (not shown here) show that no long waves are generated in the wave packet tests either.

3. Model for narrow-banded waves

Numerical models of wave blocking are either based on linear wave approximations (Shyu and Phillips 1990, Trulsen and Mei 1993), or have weak dispersive characteristics (Chen *et al.* 1998), and cannot be used to simulate the experimental results shown in this paper. We therefore seek to develop a non-linear blocking model which is valid in intermediate to deep water environments. Since the experiments show the rapid evolution of side bands near the blocking region, a numerical model for a slowly varying amplitude envelope shall be developed, by considering perturbations of a carrier wave. Almost all models describing the envelope evolution can be reduced to a Schrödinger type equation in a reference frame moving with the group velocity of the carrier wave. This approach cannot be used under blocking conditions as the group velocity goes to zero at the blocking point, and the envelope will not propagate any further into the domain.

One of the key issues in the development of such a numerical model is the nature of the roots of the dispersion relation through the blocking region. The kinematic dispersion relation for water waves riding on a depth uniform current is doppler shifted and given by

$$(\omega - kU)^2 = gk \tanh kh \tag{3.1}$$

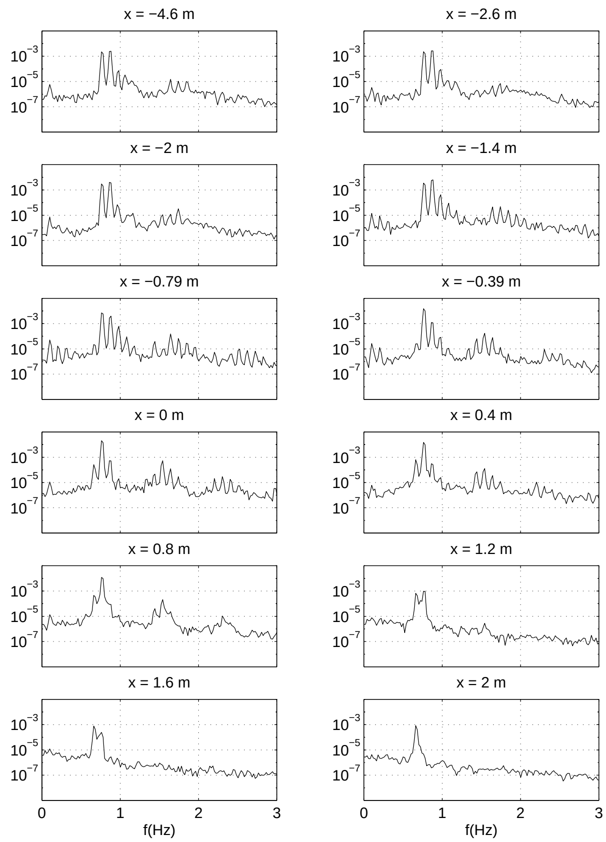

FIGURE 6. Frequency spectra corresponding to the time series shown in Figure 4 and Figure 5(Test 6). The y−*axis* is the spectral density S(f) (in m^2s)

where k is the wave number, h the water depth, ω the wave frequency and U the depth uniform current. A graphical solution of the above equation (Figure 9) shows that, in the presence of currents, the dispersion relation has two roots (denoted by **B** and **C** in the figure). As the opposing current increases, the two roots move toward each other. At the blocking point the two real-valued solutions of the dispersion relation converge. As current increases further, the two corresponding roots take on complex conjugate values, with the real part corresponding to continuing phase propagation against the current and the imaginary parts corresponding either to exponential growth or decay of the carrier wave. Assuming deep water, and solving the corresponding quadratic equation in k we get

$$k = \frac{2U\omega + g \pm g\sqrt{1 + \dfrac{4U\omega}{g}}}{2U^2} \tag{3.2}$$

k becomes complex for $U < -\dfrac{g}{4\omega}$ (which is the blocking limit based on linear theory). Figure 10 shows how the real and imaginary roots of the dispersion relation vary with the current. Beyond the blocking point two complex conjugate solutions are obtained. This leads to a complex phase function. The water surface motion η is given by

$$\eta \sim e^{i\psi}$$

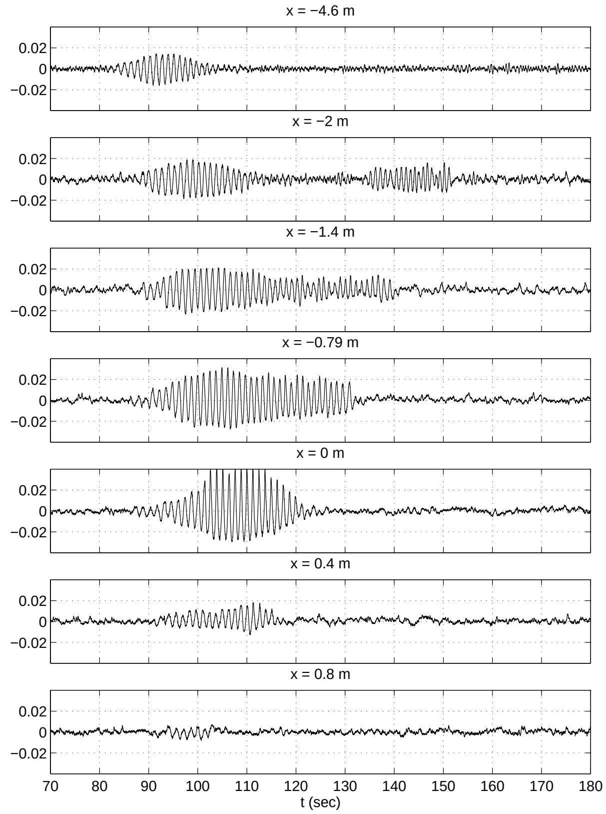

FIGURE 7. Time series of the wave packet at seven different locations in the channel (Test 6). The y−axis is surface elevation η in m

where ψ is the phase given by

$$\psi = \int (kdx - \omega dt).$$

For a complex phase the wave changes from a sinusoidal form to an exponential form, and a decaying solution can be obtained by using the appropriate root.

A numerical model has thus been developed which accounts for blocking effects by allowing the phase to be complex. The model is one-dimensional in space and has been developed for narrow channels with varying width. The orientation of the coordinate system is chosen such that the x axis lies along the channel centerline, the y axis is in the cross channel direction and the z axis points in the vertical direction. The short wave motion is in the positive x direction, while the underlying steady depth uniform current is in the opposite direction.

The governing equations for the model have been developed using a WKB perturbation expansion technique, with the difference being that the phase is allowed to be complex. The detailed derivation is outlined in appendix A. The model for a width averaged amplitude envelope, correct to the third order is given by

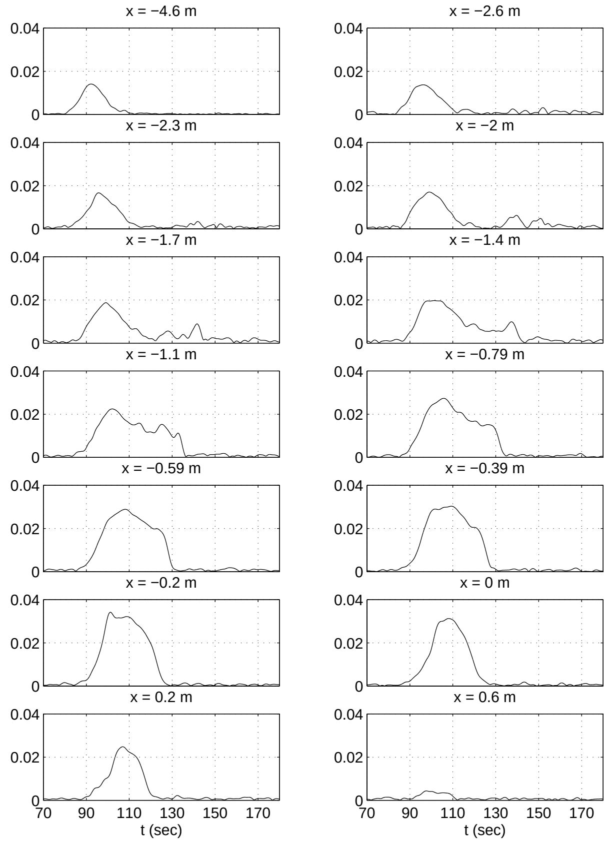

FIGURE 8. Amplitude envelope of the wave packet at 14 different locations in the channel (Test 6). The y−axis is the amplitude in m

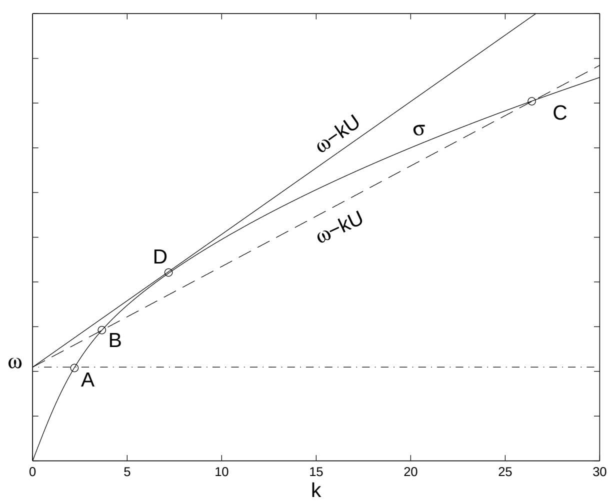

FIGURE 9. Graphical solution of the dispersion relation ('Dash Dot line' U = 0; 'Dash line' U < blocking current; 'Solid line' U = blocking current)

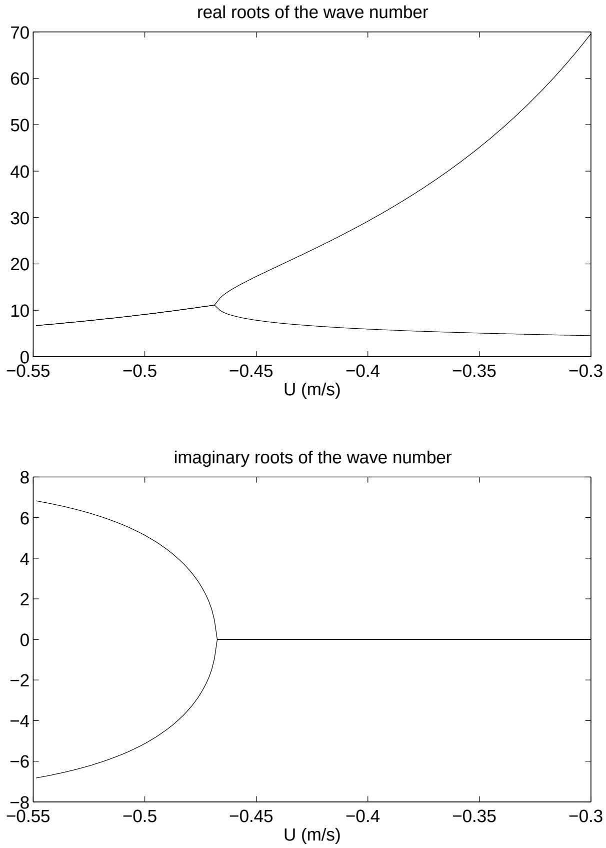

FIGURE 10. real and imaginary components of the roots of the Doppler shifted linear dispersion relation as a function of U (T = 1.2 s). The y−axis corresponds to the real (top) and imaginary (bottom) component of the wave number in m^{-1}

$$\bar{\Phi}_{1,0_{tt}} + 2U\bar{\Phi}_{1,0_{xt}} + (U^2 - g(h+\eta_c))\bar{\Phi}_{1,0_{xx}}$$
$$= \frac{\alpha g^2}{2}\left\{\Big(\frac{\sigma-\sigma^*}{|\sigma|^2}\Big)(\bar{A}_x\bar{A}^*R_1 - \bar{A}_x^*\bar{A}R_1{}^*) + \Big\{\bar{A}_x\bar{A}^*\big(\frac{R_2}{2} + R_3\big) + c.c.\Big\}\right\} \tag{3.3a}$$

$$2\bar{A}_t + 2(U+C_g)\bar{A}_x + \frac{\sigma}{b}\Big(\frac{(U+C_g)b}{\sigma}\Big)_x\bar{A} - i\sigma_{kk}\bar{A}_{xx}$$
$$- \frac{2i\sigma k\bar{A}}{g\sinh 2q}\left(\bar{\Phi}_{1,0_t} + \Big(U - \frac{g\sinh 2q}{\sigma}\Big)\bar{\Phi}_{1,0_x}\right) + 2i\alpha|\bar{A}|^2\bar{A}(gR_4 + R_5) = 0 \tag{3.3b}$$

where $q \equiv k(h+\eta_c)$, $\bar{A}$ is the width average amplitude envelope and $\bar{\Phi}_{1,0}$ is the associated width averaged long wave potential. σ, σ_{kk} and the coefficients R_1 to R_5 are given by

$$\sigma^2 = gk\tanh q \tag{3.4a}$$

$$\sigma_{kk} = \frac{2q\sigma\cosh^2 q}{k^2\sinh 2q} - \frac{C_g^2}{\sigma} - \frac{2q\sinh qC_g}{k\cosh q} \tag{3.4b}$$

$$R_1 = k^* + \frac{q|k|^2\sigma^2}{k^2} + (\sigma^*)^2(q + \tanh q) \tag{3.4c}$$

$$R_2 = \frac{k}{\sigma}(2 - \tanh^2 q) - \frac{q \tanh q}{k}\Big(\frac{k^2}{\sigma \cosh^2 q}\Big)^* \tag{3.4d}$$

$$R_3 = C_g\Big(\frac{|k|^2}{|\sigma|^2} - \frac{(k^*)^2}{2|\sigma|^2 \cosh^2 q^*} - \sigma(\sigma - \sigma^*)\Big) \tag{3.4e}$$

$$R_4 = \frac{(\sigma - \sigma^*)}{4|\sigma|^2}|k|^2(k + k^*)(\tanh q + \tanh q^*) \tag{3.4f}$$

$$\begin{aligned} R_5 = \frac{1}{8\sinh^4 q}\Big\{ & \frac{3|k|^2}{|\sigma|^2}\sigma^2(2\sigma - \sigma^*)\cosh 2q + 3k|\sigma|^2(2\sigma - \sigma^*)\sinh 2q \\ & + 3\sigma k^2(1 - 2\sinh^2 q) - \sigma^3 \sinh^2 q\Big(\frac{|\sigma|^2(1 + |\tanh q|^2)}{|\tanh q|^2} \\ & - (k \tanh q + k^* \tanh q^*)\Big) - \frac{|k|^2\sigma^* \sinh 2q(1 + 2\cosh^2 q)}{2\sinh 2q^*} \\ & - \sinh^2 q\Big(\frac{|k|^2\sigma^3}{|\sigma|^2} + \frac{k(k - k^*)}{\sigma}\sinh^2 q\Big(\frac{|k|^2}{|\sigma|^2} + |\sigma|^2\Big)\Big) \\ & + \frac{|k|^2}{|\sigma|^2}\sigma \sinh^4 q(k + k^*)(\tanh q + \tanh q^*)\Big\} \end{aligned} \tag{3.4g}$$

When there is no wave blocking then ψ, k and σ are real and (3.3) simplifies to

$$\bar{\Phi}_{1,0_{tt}} + 2U\bar{\Phi}_{1,0_{xt}} + (U^2 - g(h + \eta_c))\bar{\Phi}_{1,0_{xx}} = \alpha\Big\{\frac{\sigma^3}{2k\tanh^2 q} + \frac{C_g\sigma^2}{4\sinh^2 q}\Big\}(|A|^2)_x \tag{3.5a}$$

$$\begin{aligned} & 2\bar{A}_t + 2(U + C_g)\bar{A}_x + \frac{\sigma}{b}\Big(\frac{(U + C_g)b}{\sigma}\Big)_x\bar{A} - i\sigma_{kk}\bar{A}_{xx} - \frac{2i\sigma k\bar{A}}{g\sinh 2q}\Bigg(\bar{\Phi}_{1,0_t} \\ & + \Big(U - \frac{g\sinh 2q}{\sigma}\Big)\bar{\Phi}_{1,0_x}\Bigg) + 2i\alpha|\bar{A}|^2\bar{A}\Big(\frac{\sigma k^2(\cosh 4q + 8 - 2\tanh^2 q)}{16\sinh^4 q}\Big) = 0 \end{aligned} \tag{3.5b}$$

For a constant width (3.5) reduces to the 1-D evolution model of Turpin *et al.* (1983). Neglecting frequency dispersion and non-linear terms, and converting to an energy equation by multiplying with $\frac{1}{\rho}g\bar{A}^*$ and adding the complex conjugate of the resulting equation, we get

$$\Big(\frac{E}{\sigma}\Big)_t + \frac{1}{b}\Big(\frac{b(U + C_g)E}{\sigma}\Big)_x = 0 \tag{3.6}$$

where $E \equiv \frac{1}{2}\rho g|\bar{A}|^2$. Eqn. (3.6) is the width integrated wave action conservation principle.

3.1. *Choice of k beyond the blocking point*

We have already seen from the graphical solution of the dispersion relation in Figure 10 that beyond the blocking point we get a pair of complex conjugate roots. The choice of the wave number has to be made carefully so as to choose the decaying solution beyond the blocking point.

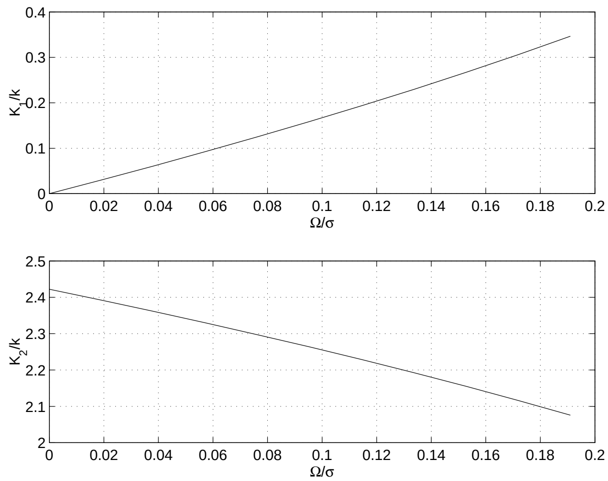

FIGURE 11. K_1 and K_2 as a function of Ω. (T = 1.2 s, U = 0.0 m/s, h = 0.5 m)

Since the surface motion is denoted by $\eta_w = \frac{A}{2}e^{i\psi} + O(\epsilon)$ a positive $Im(k)$ ($Im(f)$ refers to the imaginary part of complex function f) seems to be the appropriate choice as it leads to a decaying solution for the surface motion. However, that is only true if the wave amplitude does not change rapidly beyond the blocking point. Since the surface motion is dependent on the wave amplitude, it is necessary to study how the envelope equation varies beyond the blocking point before choosing the wave number root.

Consider a linearized version of the evolution equation (3.3) in a uniform medium (i.e. no shoaling)

$$2\bar{A}_t + 2(U + C_g)\bar{A}_x - i\sigma_{kk}\bar{A}_{xx} = 0 \tag{3.7}$$

Assuming a plane wave solution for the wave amplitude

$$\bar{A} = ae^{i(Kx-\Omega t)}$$

and substituting in (3.7) we get

$$\Omega = (U + C_g)K + K^2\frac{\sigma_{kk}}{2} \tag{3.8}$$

Solving the quadratic eqn. (3.8) for K, we get a pair of solutions

$$K_1 = \Big(\frac{-(U + C_g) + \sqrt{(U + C_g)^2 + 2\Omega\sigma_{kk}}}{\sigma_{kk}}\Big) \tag{3.9a}$$

$$K_2 = \Big(\frac{-(U + C_g) - \sqrt{(U + C_g)^2 + 2\Omega\sigma_{kk}}}{\sigma_{kk}}\Big) \tag{3.9b}$$

Figure 11 shows the plots of the two roots as a function of Ω for a wave with $T = 1.2$ s.

In the figure $K_1 \to 0$ as $\Omega \to 0$, which means that for this root the wave amplitude will be constant in space when there are no modulations in time, which makes physical sense. However, in the case of K_2 there will be spatial modulations in the wave amplitude even in the absence of any temporal variations. Furthermore, in the deep water limit, and assuming that temporal variations in amplitude are much slower than phase changes

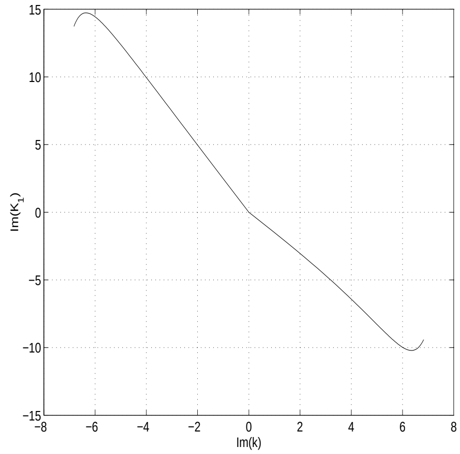

FIGURE 12. $Im(K_1)$ as a function of $Im(k)$

$(\frac{\Omega}{\sigma} \ll 1)$, the roots can be approximated as

$$K_1 \approx \frac{2k\Omega}{\sigma} \tag{3.10a}$$

$$K_2 \approx 2k\left(2 - \frac{\Omega}{\sigma}\right) \tag{3.10b}$$

which yields

$$\frac{d\Omega}{dK_1} \approx \frac{\Omega}{2k} \tag{3.11a}$$

$$\frac{d\Omega}{dK_2} \approx -\frac{\Omega}{2k} \tag{3.11b}$$

K_2 has a negative group velocity and will propagate wave energy backwards. Thus, K_2 is a spurious root to the solution, which leads to spatial modulations that propagate backwards.

A positive $Im(K_1)$ will yield a decaying solution for the wave amplitude beyond the blocking point. Using (A 48) and (A 40) $Im(K_1)$ has been plotted as a function of $Im(k)$ in Figure 12, for $\Omega \approx 0.5\mathrm{s}^{-1}$. From the figure we see that the signs of $Im(K_1)$ and $Im(k)$ are opposite, and a choice of a positive $Im(k)$ will lead to an exponential growth in the wave amplitude A. Since $|Im(K_1)| > |Im(k)|$, the growth in the amplitude will be stronger than the subsequent decay due to the complex phase, causing the waves to blow up beyond the blocking point. Thus, to simulate wave blocking we have to choose the root with a negative $Im(k)$.

3.2. *Energy dissipation due to wave breaking*

Energy dissipation due to wave breaking is introduced as an additional sink term in the envelope equation. Considering only the shoaling model we have

$$2\bar{A}_t + 2(U + C_g)\bar{A}_x + \frac{\sigma}{b}\left(\frac{(U + C_g)b}{\sigma}\right)_x \bar{A} + \gamma\bar{A} = 0 \tag{3.12}$$

where γ is the energy dissipation coefficient. The expression for γ is evaluated using the empirical dissipation term D developed for monochromatic breaking waves on opposing current by Chawla and Kirby (2002).

To compare γ with D, we first write (3.12) as an energy equation in exactly the same way as we did for (3.6)

$$\frac{1}{b}\left[\frac{\partial}{\partial x}\left(\frac{bE(U+C_g)}{\sigma}\right)\right] = -\frac{\gamma E}{\sigma} \tag{3.13}$$

where we have made the assumption of steady waves to eliminate the time derivative term. Comparing eqn. (3.13), with eqns. (7) and (12) in Chawla and Kirby (2002), we get

$$\gamma = \frac{2\beta}{\sigma\pi} g k^2 |A| \tag{3.14}$$

where, β is a coefficient to quantify energy loss due to wave breaking. Similar to a Miche's criterion used in Chawla and Kirby (2002), a slope criterion is used to determine the onset of wave breaking. But for numerical stability reasons the energy dissipation term is ramped up smoothly as waves approach the limiting slope.

4. Numerical Scheme

The set of coupled equations in (3.3) are solved using two second order finite difference schemes. The spatial coordinate x has been discretized by $x_j = j\Delta x$, while time has been discretized by $t_k = k\Delta t$.

For the long wave motion we use a backward time centered space (BTCS) numerical scheme. The derivatives are thus given by

$$\bar{\Phi}_{1,0_{tt}} = \frac{1}{(\Delta t)^2}\left(\bar{\Phi}^{k+1}_{1,0_j} + \bar{\Phi}^{k-1}_{1,0_j} - 2\bar{\Phi}^{k}_{1,0_j}\right)$$

$$\bar{\Phi}_{1,0_{xx}} = \frac{1}{(\Delta x)^2}\left(\bar{\Phi}^{k+1}_{1,0_{j+1}} + \bar{\Phi}^{k+1}_{1,0_{j-1}} - 2\bar{\Phi}^{k+1}_{1,0_j}\right)$$

$$\bar{\Phi}_{1,0_{xt}} = \frac{1}{2\Delta x\Delta t}\left(\bar{\Phi}^{k+1}_{1,0_{j+1}} - \bar{\Phi}^{k+1}_{1,0_{j-1}} - \bar{\Phi}^{k}_{1,0_{j+1}} + \bar{\Phi}^{k}_{1,0_{j-1}}\right)$$

$$\bar{A}_x = \frac{1}{2\Delta x}\left(\bar{A}^{k+1}_{j+1} - \bar{A}^{k-1}_{j+1}\right)$$

Solving for the entire spatial domain at any time step leads to a set of equations which in matrix form can be written as

$$\left[C_1\right]\left\{\bar{\Phi}^{k+1}_{1,0}\right\} = \left\{F\left(\bar{\Phi}^{k}_{1,0}, \bar{\Phi}^{k-1}_{1,0}, \quad \text{nonlinear terms in} \quad \bar{A}^{k+1}\right)\right\} \tag{4.2}$$

For the envelope equation we use a Crank-Nicolson scheme. The scheme is centered in space, and centered in time but about grid level $k+\frac{1}{2}$ with a grid spacing of $\frac{\Delta t}{2}$. The derivatives are thus given by

$$\bar{A}_t = \frac{1}{\Delta t}\left(\bar{A}^{k+1}_j - \bar{A}^{k}_j\right)$$

$$\bar{A}_x = \frac{1}{4\Delta x}\left(\bar{A}^{k+1}_{j+1} - \bar{A}^{k+1}_{j-1} + \bar{A}^{k}_{j+1} - \bar{A}^{k}_{j-1}\right)$$

$$\bar{A}_{xx} = \frac{1}{2(\Delta x)^2}\left(\bar{A}^{k+1}_{j+1} + \bar{A}^{k+1}_{j-1} - 2\bar{A}^{k+1}_j + \bar{A}^{k}_{j+1} + \bar{A}^{k}_{j-1} - 2\bar{A}^{k}_j\right)$$

Once again solving for the entire spatial domain at a particular time step leads to a set of equations which in matrix form are given by

$$\left[C_2\right]\left\{\bar{A}^{k+1}\right\} = \left\{S\left(\bar{\Phi}_{1,0}^{k+1}, \bar{\Phi}_{1,0}^{k}, \bar{A}^{k}, \quad \text{nonlinear terms in} \quad \bar{A}^{k+1}\right)\right\} \tag{4.4}$$

The coefficient matrices in (4.2) and (4.4) are tridiagonal and can be easily inverted to obtain $\bar{\Phi}_{1,0}$ and $\bar{A}$ at the new time step for all points in the spatial domain. Since the forcing vectors F and S involve terms at time step $k+1$ the solution is obtained iteratively.

4.1. *Boundary conditions*

For the long wave motion, Sommerfeld radiating boundary conditions were used at both the upwave and downwave boundaries

$$\bar{\Phi}_{1,0_t} - (U + \sqrt{gh})\bar{\Phi}_{1,0_x} = 0 \quad \text{Upwave boundary} \tag{4.5a}$$

$$\bar{\Phi}_{1,0_t} + (U + \sqrt{gh})\bar{\Phi}_{1,0_x} = 0 \quad \text{Downwave boundary} \tag{4.5b}$$

For the wave envelope equation the Sommerfeld radiating boundary condition was used for the downwave boundary while the upwave boundary condition was the prescribed wave amplitude.

$$A = a_0(t)\tanh(t) \quad \text{Upwave boundary} \tag{4.6a}$$

$$\bar{A}_t + (U + C_g)\bar{A}_x = 0 \quad \text{Downwave boundary} \tag{4.6b}$$

where the $\tanh(t)$ function is used to slowly ramp up the signal to its full value and suppress noise associated with a sudden start. The initial condition is the at rest state over the entire domain, except for the prescribed underlying steady flow field.

To test our coupled equation numerical model we simulated the propagation of a soliton. Zakharov and Shabat (1972), using an inverse scattering technique showed that solitons are a permanent form solution of the Schrödinger equation. In the absence of any wave blocking and in a uniform medium (i.e. constant depth and width) our model can be reduced to a Schrödinger equation. Thus, it should be able to propagate a soliton without changing shape. In a test case for a propagating soliton (maximum amplitude 0.05 m), the change in the maximum amplitude was less than 0.16% over a propagation distance of 150 m.

4.2. *Numerical Filter*

The contracting channel leads to the growth of numerical instabilities that propagates along the spurious root K_2. This necessitates the need for a numerical filter to damp out these instabilities. A '3 point' filter is used for this purpose (Shapiro 1970).

$$A_{new}|_{x=j\Delta x} = \gamma_f A|_{x=j\Delta x} + \frac{1-\gamma_f}{2}\left(A|_{x=(j-1)\Delta x} + A|_{x=(j+1)\Delta x}\right) \tag{4.7}$$

Detailed analysis on the need for numerical filtering and its properties are given in appendix B, where the filter has been shown to succesfully remove the spurious oscillations.

An important question is how the numerical filtering effects any of the reflected waves. According to linear theory, the reflected wave will travel back from the blocking point with a wave number given by the larger of the two roots in (3.2). Assuming plane wave oscillations of the amplitude envelope, the wave number for the spurious wave is given by the sum of K_2 (in 3.9b) and the wave number of the carrier wave (smaller of the two roots

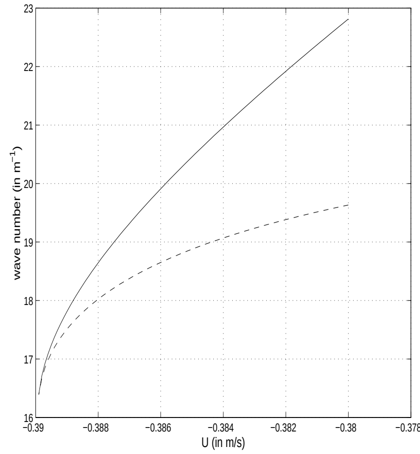

FIGURE 13. Comparison of reflected wave wave number ('solid line') and spurious oscillation wave number ('dashed line') as a function of current, close to the blocking region for T = 1.0 s. Temporal oscillation Ω in (3.9b) have been ignored while computing the spurious oscillation wave number.

in (3.2)). Figure 13 shows the two wave numbers as a function of current speed close to the linear blocking point for a 1 sec wave. At the blocking point, the spurious oscillation and the reflected wave both have the same wave number as the forward propagating carrier wave as can also be deduced from the eqns. (3.2) and (3.9b). However, away from the blocking point we see that the reflected waves are much shorter than the spurious oscillations. As a result, any numerical filter that damps out the spurious waves is also going to damp out the reflected waves as well. This is a limitation of using numerical filtering.

5. Comparison with data

For comparisons with experimental results numerical simulations were done in a domain which is linearly varying just like in the experiments. The filtering was done only until the blocking point. It should be kept in mind that since the phase function is allowed to be complex, the actual amplitude envelope is given by $|A|e^{-Im(\psi)}$, and this expression is used to compare the amplitude envelope with the data.

5.1. *Monochromatic wave tests*

For numerical simulations of monochromatic wave trains we had $\Delta x = 0.05$ m and $\Delta t = 0.005$ s. Numerical filtering was done every 10 time steps. Test 1 of the reflected wave tests was used to compare the wave blocking capabilities of the numerical model, while Tests 2 and 4 of the monochromatic breaking wave tests were used to compare model capabilities under larger amplitudes. Figure 14 shows the snapshots of the amplitude envelope at different instances in time for Test 1 of the reflected wave tests. The data has been plotted for comparison. The model picks up the features of wave blocking. Since the numerical filtering damps out both the reflected waves and the spurious scillations, the modulation of wave amplitude observed in the data is not well represented. Figures 15 and 16 shows the amplitude comparison for the larger amplitude tests (Tests 2 and 4 of the monochromatic breaking wave tests). From the plots we can see that though the model is able to block the waves, the blocking occurs earlier than in the data, with the disparity increasing with increasing wave amplitude. This is because the model uses a

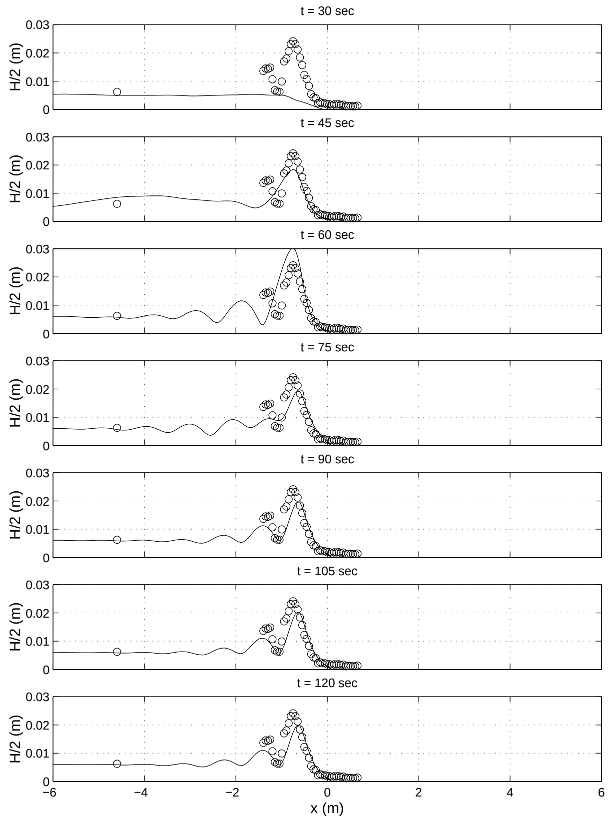

FIGURE 14. Model to data comparison of the amplitude envelope for a monochromatic wave (T = 1.2 s, H = 0.0125 m, γ_f = 0.7)

linear dispersion relation (A 52) to predict the location of the blocking point, while the actual blocking occurs later due to amplitude dispersion effects. The importance of non-linear dispersion in wave blocking was pointed out in Chawla and Kirby (2002), and the inability of the model to predict this effect is a fairly strong limitation of the model.

5.2. *Wave group tests*

For the experimental studies on wave groups, the groups were constructed by superposing two monochromatic waves having the same amplitude but slightly different frequencies. For the model, similar wave groups can be constructed by modulating a carrier wave. To correspond with the wave groups of Test 6, the carrier wave has a wave period $T = 1.22$ s, and the amplitude forced at the boundary is a sine wave with a period $T_a = 19.92$ s. For the simulations we used $\Delta x = 0.05$ m and $\Delta t = 0.012$ s, which corresponds to the sampling frequency at which the data was collected in the experiment.

A comparison of the model and data surface elevation time series at the first gage ($x = -4.6$ m) is shown in Figure 17. In the experiments the waves have evolved by the time they reach the first gage and do not strictly consist of just two components (see Figure 6), hence the mismatch between the model and data time series. Nevertheless, the wave groups generated by the model and data are fairly similar at this location. Figures 18 and 19 show the evolution of the amplitude envelopes for the model and data as a function of time and space. In the experiments we observed that the individual wave components of the wave group are blocked at their respective blocking points and the

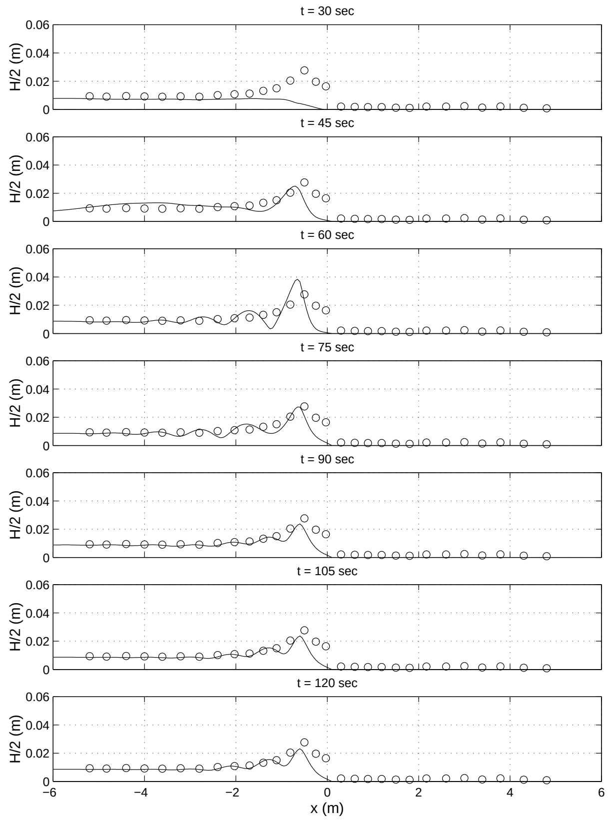

FIGURE 15. Model to data comparison of the amplitude envelope for a monochromatic wave (T = 1.2 s, H = 0.018 m, γ_f = 0.70)

time series goes from being groupy to becoming monochromatic around $x = 0$ m, by which time the shorter wave component is blocked, and then being completely blocked by $x = 1.6$ m. In the model such a transformation would be expected to occur even earlier since the model, using linear theory, predicts earlier wave blocking. However, the comparisons show that the waves tend to remain groupy in the model even when they are being transformed in the data, and instead of the individual wave components being blocked at their respective blocking points, the wave group gets blocked at the blocking point of the carrier wave. The blocking characteristics of the model and data can be seen from the spectrum comparisons shown in Figure 20. While wave blocking in the data occurs selectively, with the higher frequencies getting blocked first, wave blocking in the model occurs at the blocking point of the carrier frequency, with considerable energy present in higher frequency components past their linear blocking limits.

This limitation of the model to not separately block parts of the frequency spectrum also prevents the model to reproduce the experimental results of monochromatic wave tests in which it was seen that for bigger wave conditions, wave blocking was prevented because of the transfer of wave energy from the principal wave component to the lower side band instabilities (Chawla and Kirby 2002).

5.3. *Wave packet tests*

For the wave packet tests, wave packets in the experiments were generated with the help of Gaussian shaped frequency spectra. The wave packet in the model was created by

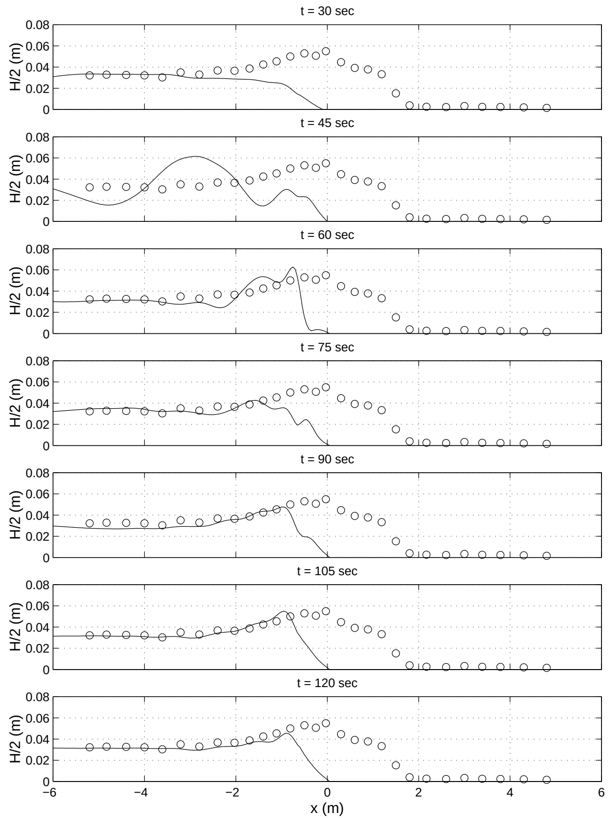

FIGURE 16. Model to data comparison of the amplitude envelope for a monochromatic wave (T = 1.2 s, H = 0.066 m, γ_f = 0.70)

modulating the wave amplitude using a half-sine wave with a wave period $T_a = 19.92$ s. The wave period of the carrier wave was 1.22 s. The time step Δt was set to 0.01 s to match with the sampling frequency for the experiments. A strong filter ($\gamma_f = 0.6$ and filtering every 5 time steps) was used to remove all the numerical instabilities.

Figure 21, shows the comparison of the model and data surface elevation time series at the first gage ($x = -4.6$ m). Both time series are very similar at this position, though the amplitude envelope in the data is less symmetrical when compared to that of the model. Following the analysis done for the experimental results in Figure 8, we again use wavelet transforms to obtain the amplitude envelope for the numerical simulation. Figure 22 shows the comparison between the amplitude envelope for the model and the data. Cross correlation between the model and data elevation time series at the first gage was used to remove the temporal lag between the model and data results. Just like in the experimental results, a reflected wave packet can be observed between $x = -2.6$ m and $x = -0.59$ m. The separation distance between the incident and reflected wave packets at any particular gage location is greater in the experimental data as compared to model simulations because the blocking point in the experiments is further away due to non-linear dispersion effects. The greater dissipation in reflected wave packets of the data is probably due to capillary dissipative processes in the very short reflected waves that are not simulated in the model.

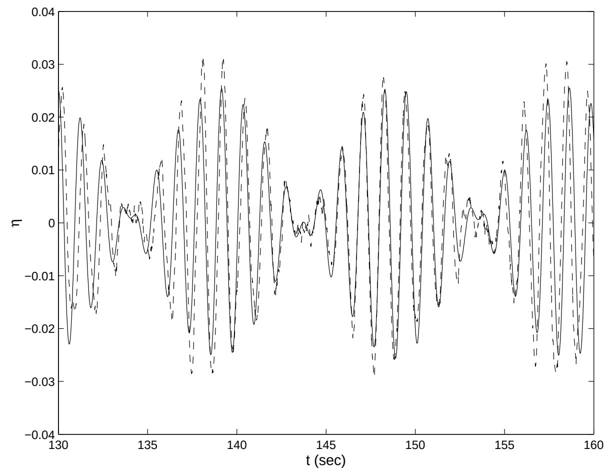

FIGURE 17. Model ('solid line') to data ('dashed line') comparisons of surface elevation time series at gage 1 ($x = -4.6$ m) for wave groups Test 6

6. Conclusions

A weakly non-linear model has been developed for the evolution of the envelope of a narrow-banded spectrum propagating in strong currents. The model has been developed for channels of varying width and depth. Beyond the blocking point, the roots of the dispersion relation branch out to give a pair of complex conjugate roots. Thus, the wave changes from a progressive periodic form to an exponentially damped form. Choosing the correct root leads to the decay of wave motion beyond the blocking point. In the absence of wave blocking and for a channel of constant width, our model can be reduced to the model of Turpin *et al.* (1983).

The model consists of a pair of coupled equations for the wave envelope and the long wave motion. Usually in the literature the long wave motion is integrated out to yield just a single equation. However, due to the complex nature of the coefficients this is not possible in our case and we have to solve a coupled system of equations. The numerical scheme consists of a BTCS scheme for the long wave equation and a Crank-Nicolson scheme for the envelope equation. Numerical tests on the propagation of a soliton have shown that the model works well. The governing envelope equation has two roots, one in which the wave energy is transported in the direction of propagation of the carrier wave, and a second spurious root in which the energy is transported in the opposite direction. In the uniform channel, the model picks up the correct root. However, within a rapid channel transition with increasing opposing current, the model is unstable. The strength of the instability grows with the rate at which the group velocity is decreasing and the disturbance is propagated backwards as the spurious root. To counteract the growth of the unstable mode a 3 point filter is used in the model.

The choice of the correct root to damp out the waves beyond the blocking point is not straightforward. The apparent choice is the wave number with the positive imaginary component, which will lead to decay of the surface wave amplitude for a fixed reference wave amplitude. However, the choice of this root actually causes the complex wave amplitude to increase exponentially. Since the increase in the amplitude is greater than the decay due to the phase function, the overall solution will blow up. Therefore, the correct choice to simulate wave blocking is the root with the negative imaginary wave number.

Numerical simulations with very small amplitude monochromatic waves and wave pack-

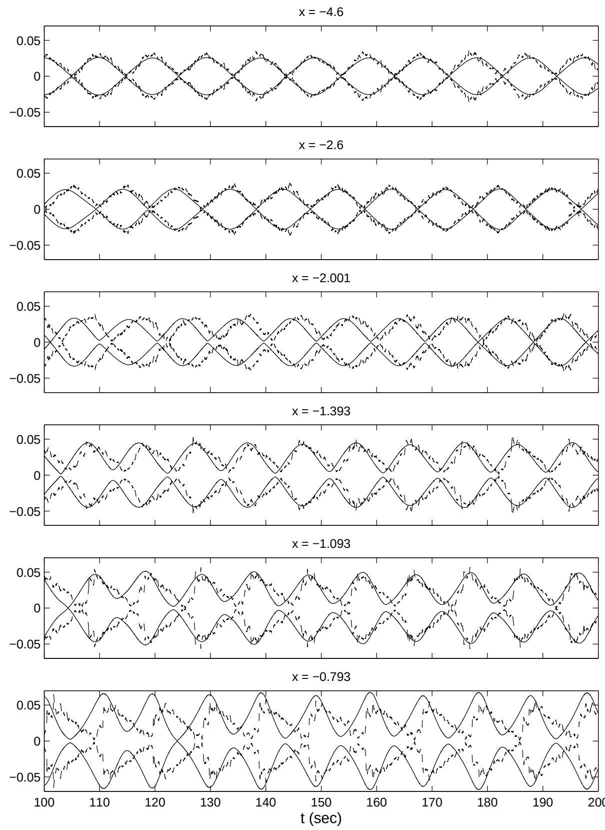

FIGURE 18. Model ('solid line') to data ('dashed line') comparisons of the amplitude envelope at six different locations ($\gamma_f = 0.6$)

ets show that the model does a reasonable job in blocking the waves. However the model has a few major limitations. The development of spurious backward propagating numerical instabilities requires the implementation of a numerical filter which unfortunately also damps out the shorter reflected waves. The model also predicts the blocking point based on the linear dispersion relation and cannot account for non-linear dispersive effects. The experimental results reported in Chawla and Kirby (2002) have shown that due to the sharp steepening of the waves prior to the blocking point, the non-linear terms in the dispersion relation become important and the linear dispersion relation does a poor job of predicting the position of wave blocking. Another major limitation of the model is that blocking occurs at the blocking point of the carrier wave. However, experimental observations both in the blocking of monochromatic wave trains with side bands and in the blocking of wave groups have shown that this is not the case, and the waves are blocked selectively at the blocking points for the individual wave components in the spectrum. This inability of the model to block the wave components of the spectrum separately means that the model is unable to simulate wave propagation with transfer of energy into lower side bands as observed in the monochromatic wave tests. The modeling exercise carried out in this paper shows that the wave blocking process can be simulated by allowing the wave number to be complex. The limitations in the model indicates the need for a spectral solution along the lines of the non-linear integro-differential model of Zakharov (1968) which treats the dynamics of each frequency component separately.

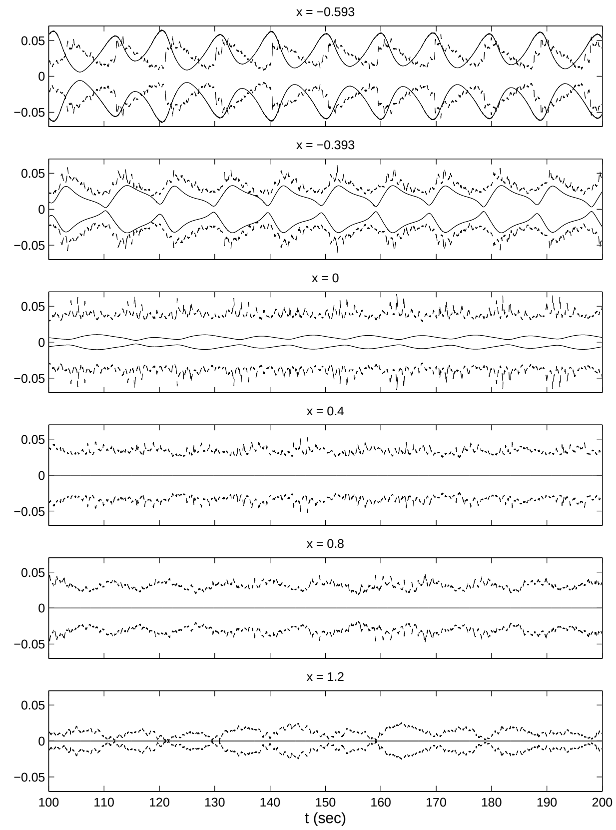

FIGURE 19. Model ('solid line') to data ('dashed line') comparisons of the amplitude envelope at six different locations ($\gamma_f = 0.6$)

The wave frequency also needs to be perturbed (Lin and Perrie 1997) so as to retrieve a non-linear dispersive relation.

Acknowledgments

This research has been sponsored by the NOAA Office of Sea Grant, Department of Commerce, under Grant No. NA56RG0147 (Project No. R/OE-21). The U.S. Government is authorized to produce and distribute reprints for governmental purposes, not withstanding any copyright notation that may appear heron.

Appendix A. Derivation of the evolution equation

The boundary value problem for irrotational fluid flow in terms of a velocity potential $\acute{\Phi}$ is given by

$$\acute{\Phi}_{\acute{x}\acute{x}} + \acute{\Phi}_{\acute{y}\acute{y}} + \acute{\Phi}_{\acute{z}\acute{z}} = 0; \quad -\acute{h} \le \acute{z} \le \acute{\eta} \tag{A 1a}$$

$$\acute{\Phi}_{\acute{z}} + \acute{h}_{\acute{x}}\acute{\Phi}_{\acute{x}} + \acute{h}_{\acute{y}}\acute{\Phi}_{\acute{y}} = 0; \quad \acute{z} = -\acute{h} \tag{A 1b}$$

$$\acute{\eta} = -\frac{\acute{\Phi}_{\acute{t}}}{g} - \frac{1}{2g}\Big(\acute{\Phi}_{\acute{x}}^2 + \acute{\Phi}_{\acute{y}}^2 + \acute{\Phi}_{\acute{z}}^2\Big); \quad \acute{z} = \acute{\eta} \tag{A 1c}$$

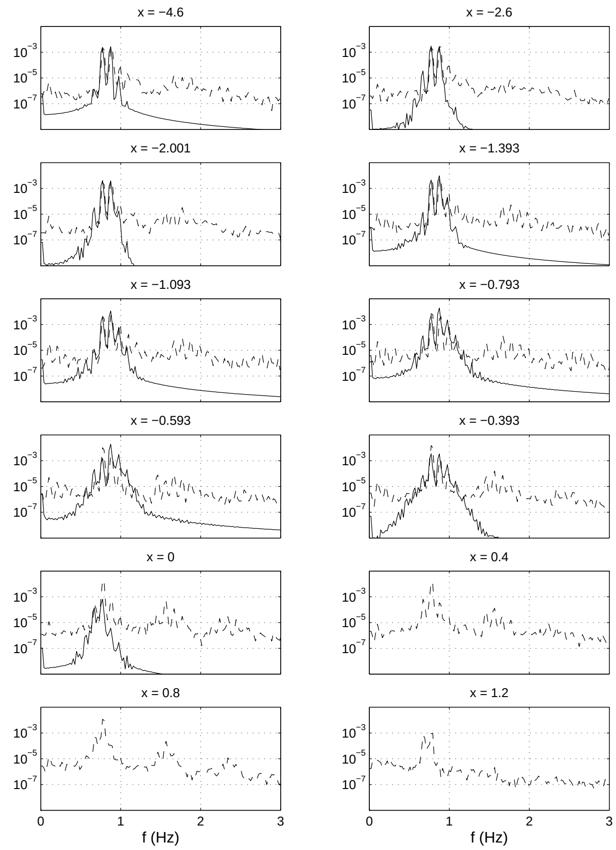

FIGURE 20. Model ('solid line') to data ('dashed line') comparisons of the frequency spectra for Test 6

$$\begin{aligned}&\acute{\Phi}_{\acute{t}\acute{t}} + g\acute{\Phi}_{\acute{z}} + \left(\acute{\Phi}^2_{\acute{x}} + \acute{\Phi}^2_{\acute{y}} + \acute{\Phi}^2_{\acute{z}}\right)_{\acute{t}} \\ &+ \frac{1}{2}\left\{\acute{\Phi}_{\acute{x}}\frac{\partial}{\partial\acute{x}} + \acute{\Phi}_{\acute{y}}\frac{\partial}{\partial\acute{y}} + \acute{\Phi}_{\acute{z}}\frac{\partial}{\partial\acute{z}}\right\}\left(\acute{\Phi}^2_{\acute{x}} + \acute{\Phi}^2_{\acute{y}} + \acute{\Phi}^2_{\acute{z}}\right) = 0; \quad \acute{z} = \acute{\eta}\end{aligned} \tag{A 1d}$$

$$\acute{\Phi}_{\acute{y}} = \pm\acute{b}_{\acute{x}}\acute{\Phi}_{\acute{x}}; \quad \acute{y} = \pm\acute{b} \tag{A 1e}$$

where $2\acute{b}$ is the channel width and $\acute{\eta}$ is the surface displacement due to the combined effect of current and waves.

We now nondimensionalize the problem using the following scaling

$$\eta = \frac{\acute{\eta}}{a}; \qquad \Phi = \frac{\epsilon k_0^2}{\sqrt{gk_0}}\acute{\Phi} \tag{A 2}$$
$$t = \sqrt{gk_0}\acute{t};\ (x, y, z, h, b) = k_0(\acute{x}, \acute{y}, \acute{z}, \acute{h}, \acute{b})$$

where a is the measure of wave amplitude, k_0 is the measure of wave number and $\epsilon = k_0 a$ is a nonlinearity parameter.

The resulting B.V.P. is given by

$$\Phi_{xx} + \Phi_{yy} + \Phi_{zz} = 0; \quad -h \le z \le \epsilon\eta \tag{A 3a}$$

$$\Phi_z + h_x\Phi_x + h_y\Phi_y = 0; \quad z = -h \tag{A 3b}$$

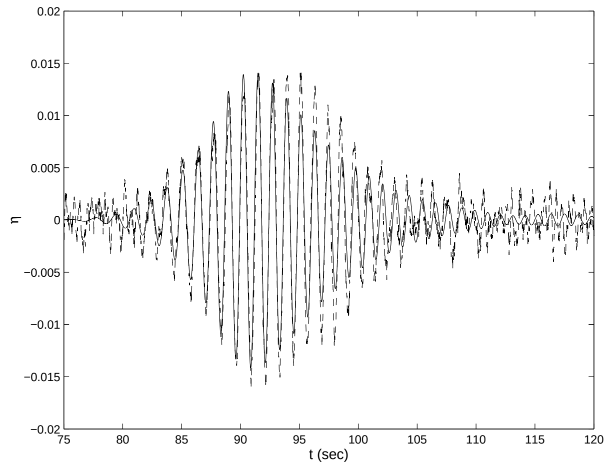

FIGURE 21. Model ('solid line') to data ('dashed line') comparisons of surface elevation time series at gage 1 ($x = -4.6$ m) for wave packets Test 6

$$\eta = -\Phi_t - \frac{\epsilon}{2}\left(\Phi_x^2 + \Phi_y^2 + \Phi_z^2\right); \quad z = \epsilon\eta \tag{A 3c}$$

$$\begin{aligned} &\Phi_{tt} + \Phi_z + \epsilon\left(\Phi_x^2 + \Phi_y^2 + \Phi_z^2\right)_t \\ &+ \frac{\epsilon^2}{2}\left\{\Phi_x \frac{\partial}{\partial x} + \Phi_y \frac{\partial}{\partial y} + \Phi_z \frac{\partial}{\partial z}\right\}\left(\Phi_x^2 + \Phi_y^2 + \Phi_z^2\right) = 0; \quad z = \epsilon\eta \end{aligned} \tag{A 3d}$$

$$\Phi_y = \pm b_x \Phi_x; \quad y = \pm b \tag{A 3e}$$

Since the waves are propagating in the positive x direction, we have a fast scale in x and t over which the phase of wave motion changes and a slower scale over which the wavenumber and wave amplitude changes. Across the channel there are no fast scales. Using stretched coordinates we thus have

$$x = x + \frac{X_1}{\epsilon} + \frac{X_2}{\epsilon^2} + \cdots \tag{A 4a}$$

$$t = t + \frac{T_1}{\epsilon} + \frac{T_2}{\epsilon^2} + \cdots \tag{A 4b}$$

$$y = \frac{Y_1}{\epsilon} + \frac{Y_2}{\epsilon^2} + \cdots \tag{A 4c}$$

Furthermore, since we are studying the interactions between an $O(1)$ current and wave motion, we can write Φ and η as

$$\Phi = \Phi_c + \epsilon\Phi_w \tag{A 5a}$$

$$\eta = \eta_c + \epsilon\eta_w \tag{A 5b}$$

where the sub-scripts c and w correspond to current and wave motion respectively.

A.1. *Solution for current motion*

Assuming that the current is steady and uniform in depth, and that both the channel geometry and depth averaged current U are a function of the slow coordinate X_2, we can

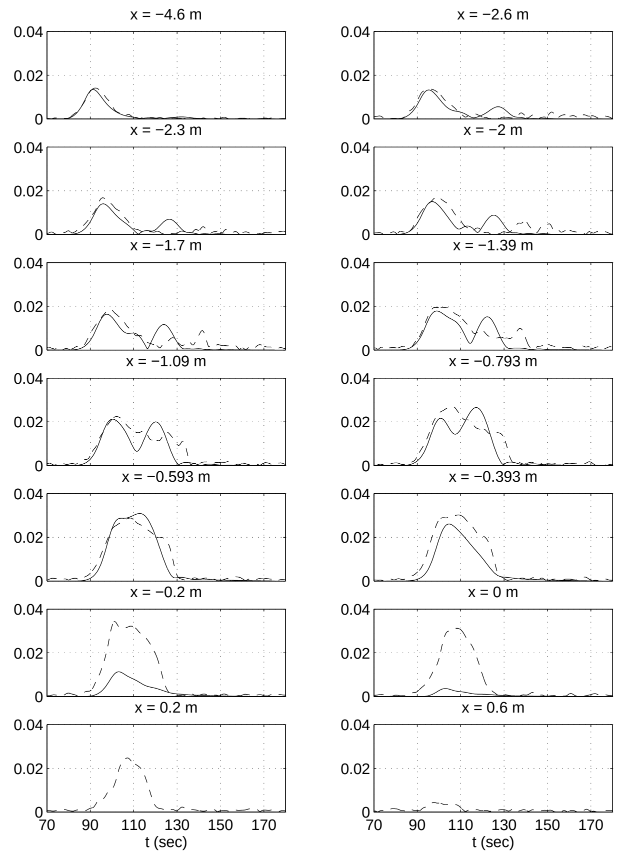

FIGURE 22. Model ('solid line') to data ('dashed line') comparisons of the amplitude envelope as a function of space and time for wave packet Test 6

write Φ_c as

$$\Phi_c = \frac{1}{\epsilon^2}\int U(X_2)dX_2 + \tilde{\Phi}_c(X_2, Y_1, Y_2, z) \tag{A 6}$$

The resulting boundary value problem for current motion in the stretched coordinate system is then given by

$$\epsilon^2 U_{X_2} + \epsilon^2 \tilde{\Phi}_{c_{Y_1 Y_1}} + \tilde{\Phi}_{c_{zz}} = 0; \quad -h \le z \le \eta_c \tag{A 7a}$$

$$\tilde{\Phi}_{c_z} = -\epsilon^2 U h_{X_2}; \quad z = -h \tag{A 7b}$$

$$\eta_c = -\frac{1}{2}\Big(U^2 + \epsilon^2(\tilde{\Phi}_{c_{Y_1}})^2 + (\tilde{\Phi}_{c_z})^2\Big); \quad z = \eta_c \tag{A 7c}$$

$$\epsilon^2\Big(\eta_{c_{X_2}} U + \eta_{c_{Y_1}}\tilde{\Phi}_{c_{Y_1}}\Big) = \tilde{\Phi}_{c_z}; \quad z = \eta_c \tag{A 7d}$$

$$\tilde{\Phi}_{c_{Y_1}} = \pm\epsilon b_{X_2} U; \quad Y_1 = \pm\epsilon b \tag{A 7e}$$

From the B.V.P. it is clear that the vertical velocity $\tilde{\Phi}_{c_z}$ is $O(\epsilon^2)$. We can thus write $\tilde{\Phi}_c$ as

$$\tilde{\Phi}_c = \tilde{\Phi}_{c1}\Big(X_2, Y_1, Y_2\Big) + \epsilon^2\tilde{\Phi}_{c2}\Big(X_2, z\Big)$$

Substituting the above expression in (A 7) and solving the B.V.P. by first integrating out the Y_1 dependency using the lateral boundary conditions, we get

$$\tilde{\Phi}_{c1} = \frac{Ub_{X_2}}{b}\frac{(Y_1)^2}{2} \tag{A 8a}$$

$$\tilde{\Phi}_{c2} = -\frac{(Ub)_{X_2}}{b}\frac{(z+h)^2}{2} - Uh_{X_2}z \tag{A 8b}$$

and the combined expression for Φ_c is given by

$$\Phi_c = \frac{1}{\epsilon^2}\int U(X_2)dX_2 + \frac{Ub_{X_2}}{b}\frac{(Y_1)^2}{2} - \epsilon^2\Big(\frac{(Ub)_{X_2}}{b}\frac{(z+h)^2}{2} + Uh_{X_2}z\Big) \tag{A 9}$$

From (A 9) it is clear that the horizontal velocity along the channel has variations in depth and across the channel. However, for our experimental setup these variations were less than 1%. Substituting (A 9) in the surface boundary conditions yields

$$\eta_c = -\frac{U^2(X_2)}{2} + O(\epsilon^4) \tag{A 10a}$$

$$(Ub(h+\eta_c))_{X_2} = O(\epsilon^4) \tag{A 10b}$$

A.2. *Solution for the combined wave-current interaction*

Substituting (A 5) in (A 3), doing a Taylor series expansion about the current surface $z = \eta_c$ and separating the B.V.P. for the steady current (eqn. A 7), we get a resulting B.V.P. for the combined wave-current interaction

$$\Phi_{wxx} + \Phi_{wyy} + \Phi_{wzz} = 0; \quad -h \le z \le \epsilon\eta_w \tag{A 11a}$$

$$\Phi_{wz} + h_x\Phi_{wx} = 0; \quad z = -h \tag{A 11b}$$

$$\begin{aligned}\eta_w = &- \Phi_{wt} - \frac{\epsilon}{2}\Big((\frac{\Phi_{cx}}{\epsilon} + \Phi_{wx})^2 + (\frac{\Phi_{cy}}{\epsilon} + \Phi_{wy})^2 + (\frac{\Phi_{cz}}{\epsilon} + \Phi_{wz})^2\Big) \\ &+ \frac{1}{2\epsilon}\Big(\Phi_{cx}^2 + \Phi_{cy}^2 + \Phi_{cz}^2\Big); \quad z = \epsilon\eta_w\end{aligned} \tag{A 11c}$$

$$\begin{aligned}&\Phi_{wtt} + \Phi_{wz} + \eta_w\Phi_{c_{zz}} + \epsilon\Big((\frac{\Phi_{cx}}{\epsilon} + \Phi_{wx})^2 + (\frac{\Phi_{cy}}{\epsilon} + \Phi_{wy})^2 + (\frac{\Phi_{cz}}{\epsilon} + \Phi_{wz})^2\Big)_t \\ &+ \frac{\epsilon^2}{2}\Big\{(\frac{\Phi_{cx}}{\epsilon} + \Phi_{wx})\frac{\partial}{\partial x} + (\frac{\Phi_{cy}}{\epsilon} + \Phi_{wy})\frac{\partial}{\partial y} + (\frac{\Phi_{cz}}{\epsilon} + \Phi_{wz})\frac{\partial}{\partial z}\Big\} \\ &\Big((\frac{\Phi_{cx}}{\epsilon} + \Phi_{wx})^2 + (\frac{\Phi_{cy}}{\epsilon} + \Phi_{wy})^2 + (\frac{\Phi_{cz}}{\epsilon} + \Phi_{wz})^2\Big) - \\ &\frac{\epsilon^2}{2}\Big\{\frac{\Phi_{cx}}{\epsilon}\frac{\partial}{\partial x} + \frac{\Phi_{cy}}{\epsilon}\frac{\partial}{\partial y} + \frac{\Phi_{cz}}{\epsilon}\frac{\partial}{\partial z}\Big\}\Big((\frac{\Phi_{cx}}{\epsilon})^2 + (\frac{\Phi_{cy}}{\epsilon})^2 + (\frac{\Phi_{cz}}{\epsilon})^2\Big) = 0; \quad z = \epsilon\eta_w\end{aligned} \tag{A 11d}$$

$$\Phi_{wy} = \pm b_x\Phi_{wx}; \quad y = \pm b \tag{A 11e}$$

Substituting the stretched coordinates (A 4), the velocity potential for current (A 9) and perturbing the wave motion using the small parameter ϵ

$$\Phi_w = \Phi_1 + \epsilon\Phi_2 + \epsilon^2\Phi_3 \tag{A 12a}$$

$$\eta_w = \eta_1 + \epsilon\eta_2 + \epsilon^2\eta_3 \tag{A 12b}$$

the nonlinear B.V.P. can be reduced to a set of linear B.V.P.s at different orders of ϵ. For compactness the following definitions shall be used

$$D \equiv \frac{\partial}{\partial t} + U\frac{\partial}{\partial x} \tag{A 13a}$$

$$\Gamma \equiv D^2 + \frac{\partial}{\partial z} \tag{A 13b}$$

$$D_1 \equiv \frac{\partial}{\partial T_1} + U\frac{\partial}{\partial X_1} \tag{A 13c}$$

$$D_2 \equiv \frac{\partial}{\partial T_2} + U\frac{\partial}{\partial X_2} \tag{A 13d}$$

$$\nabla \equiv \left(\frac{\partial}{\partial x}, \frac{\partial}{\partial z}\right) \tag{A 13e}$$

and the corresponding B.V.P.s for the first three orders of ϵ are given by

$$\Phi_{nxx} + \Phi_{nzz} = F_n; \quad -h \le z \le 0, \quad n = 1,2,3 \tag{A 14a}$$

$$\Phi_{nz} = G_n; \quad z = -h, \quad n = 1,2,3 \tag{A 14b}$$

$$\eta_n = K_n; \quad z = \eta_c, \quad n = 1,2,3 \tag{A 14c}$$

$$\Gamma\Phi_n = J_n; \quad z = \eta_c, \quad n = 1,2,3 \tag{A 14d}$$

$$\Phi_{nY_1} = H_n; \quad Y_1 = \pm\epsilon b, \quad n = 1,2 \tag{A 14e}$$

where the forcing terms are given by

$$F_1 = 0 \tag{A 15a}$$

$$F_2 = -2\Phi_{1xX_1} \tag{A 15b}$$

$$F_3 = -\left(\Phi_{1X_1X_1} + \Phi_{1Y_1Y_1}\right) - \left(\Phi_{1xX_2} + \Phi_{1X_2x}\right) - 2\Phi_{2xX_1} \tag{A 15c}$$

$$G_1 = 0 \tag{A 16a}$$

$$G_2 = 0 \tag{A 16b}$$

$$G_3 = -h_{X_2}\Phi_{1x} \tag{A 16c}$$

$$H_1 = 0 \tag{A 17a}$$

$$H_2 = \pm b_{X_2}\Phi_{1x} \tag{A 17b}$$

$$K_1 = -D\Phi_1 \tag{A 18a}$$

$$K_2 = -D\Phi_2 - D_1\Phi_1 - \frac{1}{2}\left(\nabla\Phi_1 \cdot \nabla\Phi_1\right) - \eta_1 D\Phi_{1z} \tag{A 18b}$$

$$\begin{aligned} K_3 = &- D\Phi_3 - D_1\Phi_2 - D_2\Phi_1 - \eta_1\left(D_1\Phi_{1z} + D\Phi_{2z} + \frac{1}{2}\left(\nabla\Phi_1 \cdot \nabla\Phi_1\right)_z\right) \\ &- \eta_2 D\Phi_{1z} - \frac{\eta_1^2}{2}D\Phi_{1zz} - \left(\Phi_{1x}\Phi_{1X_1} + \Phi_{1x}\Phi_{2x} + \Phi_{1z}\Phi_{2z}\right) - U\frac{b_{X_2}}{b}Y_1\Phi_{1Y_1} \\ &+ U\eta_{cX_2} \end{aligned}$$

(A 18c)

$$J_1 = 0 \tag{A 19a}$$

$$J_2 = -2DD_1\Phi_1 - D\big(\nabla\Phi_1\cdot\nabla\Phi_1\big) - \eta_1\Gamma\Phi_{1_z} \tag{A 19b}$$

$$\begin{aligned} J_3 =& -2U\frac{b_{X_2}}{b}Y_1D\Phi_{1_{Y_1}} + \eta_1\frac{(Ub)_{X_2}}{b} - D_2D\Phi_1 - DD_2\Phi_1 - D_1^2\Phi_1 + \eta_{c_{X_2}}\Phi_{1_x} \\ &- 2DD_1\Phi_2 - D_1\big(\nabla\Phi_1\cdot\nabla\Phi_1\big) - 2D\Big(\Phi_{1_x}\Phi_{1_{X_1}} + \Phi_{1_x}\Phi_{2_x} + \Phi_{1_z}\Phi_{2_z}\Big) \\ &- \frac{1}{2}\nabla\Phi_1\cdot\nabla\big(\nabla\Phi_1\cdot\nabla\Phi_1\big) - \eta_1\Big(2DD_1\Phi_1 + \Gamma\Phi_2 + D\big(\nabla\Phi_1\cdot\nabla\Phi_1\big)\Big)_z \\ &- \eta_2\Gamma\Phi_{1_z} - \frac{\eta_1^2}{2}\Gamma\Phi_{1_{zz}} \end{aligned} \tag{A 19c}$$

The first order solution of (A 14) is the linear solution for a propagating wave. Due to the presence of nonlinear forcing terms at higher orders in the surface boundary conditions, we expand the velocity potential using a WKB expansion

$$\Phi_n = \Phi_{n,0} + \Big(\sum_{m=1}^{m=n}\Phi_{n,m}e^{im\psi} + c.c.\Big) \tag{A 20}$$

where $c.c.$ is the complex conjugate and ψ is the phase function given by

$$\psi = \int (k(X_2)dx - \omega dt) \tag{A 21}$$

Thus

$$k = \psi_x \quad ; \quad \omega = -\psi_t \tag{A 22}$$

ω remains constant through the domain but k varies with the current and beyond the blocking point k becomes complex. The solution thus changes from a propagating wave form to an exponentially decaying one. Therefore, to propagate the solution through the blocking region, the phase function ψ is allowed to be complex. The forcing terms in the boundary value problem are also expanded using the WKB expansion. Substituting the expansion in (A 14) we get

$$\left(\frac{\partial^2}{\partial z^2} - m^2k^2\right)\Phi_{n,m} = F_{n,m}; \quad -h \le z \le 0 \tag{A 23a}$$

$$\Phi_{n,m_z} = G_{n,m}; \quad z = -h \tag{A 23b}$$

$$\Phi_{n,m_{Y_1}} = G_{n,m}; \quad y = \pm b \tag{A 23c}$$

$$\left(\frac{\partial}{\partial z} - m^2\sigma^2\right)\Phi_{n,m} = J_{n,m}; \quad z = \eta_c \tag{A 23d}$$

$$\eta_{n,m} = K_{n,m}; \quad z = \eta_c \tag{A 23e}$$

where

$$\sigma \equiv \omega - kU \tag{A 24}$$

Eqn (A 23) has to be solved sequentially for all m at a particular n before going to the next n level. For $n \geq 2$ there are two special cases.

<u>$m = 0$</u> : The governing equation is given by

$$\Phi_{n,0_{zz}} = F_{n,0} \tag{A 25}$$

Integrating (A 25) in depth and using the boundary conditions we get

$$\int_{-h}^{\eta_c} F_{n,0} dz = J_{n,0} - G_{n,0} \tag{A 26}$$

<u>$m = 1$</u> : The boundary value problem is given by

$$\left(\frac{\partial^2}{\partial z^2} - k^2\right)\Phi_{n,1} = F_{n,1}; \quad -h \leq z \leq \eta_c \tag{A 27a}$$

$$\Phi_{n,1_z} = G_{n,1}; \quad z = -h \tag{A 27b}$$

$$\left(\frac{\partial}{\partial z} - \sigma^2\right)\Phi_{n,1} = J_{n,1}; \quad z = \eta_c \tag{A 27c}$$

$$\eta_{n,1} = K_{n,1}; \quad z = \eta_c \tag{A 27d}$$

The homogeneous solution to (A 27) is a freely propagating wave governed by the linearized problem. To prevent secular terms, the inhomogeneous solution must satisfy a solvability condition which is given by

$$\int_{-h}^{\eta_c} \Phi_{1,1} F_{n,1} dz = \Phi_{1,1} J_{n,1}\Big|_{z=\eta_c} - \Phi_{1,1} G_{n,1}\Big|_{z=-h} \tag{A 28}$$

The two solvability conditions (A 26) and (A 28) yield the evolution equations for the wave amplitude and the corresponding long wave motion.

A.2.1. *First order solution*

The forcing terms at the lowest order are given by

$$F_1 = 0 \quad ; \quad G_1 = 0 \quad ; \quad J_1 = 0$$

At $m = 0$

$$\Phi_{1,0_z} = 0$$

Thus,

$$\Phi_{1,0} = \Phi_{1,0}(X_1, X_2, Y_1, Y_2, T_1, T_2, \cdots) \tag{A 29}$$

At $m = 1$ the boundary value problem is

$$\begin{aligned} \left(\frac{\partial^2}{\partial z^2} - k^2\right)\Phi_{1,1} &= 0; \quad -h \leq z \leq \eta_c \\ \Phi_{1,1_z} &= 0; \quad z = -h \\ \left(\frac{\partial}{\partial z} - \sigma^2\right)\Phi_{1,1} &= 0; \quad z = \eta_c \end{aligned} \tag{A 30}$$

which yields the linear solution for a propagating wave

$$\Phi_{1,1} = -\frac{iA}{2\sigma}\Big(\frac{\cosh Q}{\cosh q}\Big) \tag{A 31a}$$

$$\sigma^2 = k\tanh q \tag{A 31b}$$

where A is the wave amplitude, and the following definitions have been used for compactness

$$Q \equiv k(z+h) \qquad q \equiv k(h+\eta_c) \tag{A 32}$$

Substituting the solution for Φ_1 in the forcing term for η_1 yields at the different harmonics

$$\eta_{1,0} = 0 \tag{A 33a}$$

$$\eta_{1,1} = \frac{A}{2} \tag{A 33b}$$

A.2.2. *Second order solution*

Using the solutions at $n = 1$, the forcing terms at this order can be determined and are given by

$$F_{2,0} = 0 \quad ; \quad F_{2,1} = -\frac{kA_{X_1}}{\sigma}\Big(\frac{\cosh Q}{\cosh q}\Big) \quad ; \quad F_{2,2} = 0$$

$$G_{2,0} = 0 \quad ; \quad G_{2,1} = 0 \quad ; \quad G_{2,2} = 0$$

$$J_{2,0} = \alpha|A|^2\Bigg\{\Big(\frac{i\sigma^3}{4\sinh^2 q} + c.c.\Big) - \frac{i\Big(\sigma-\sigma^*\Big)|\sigma|^2}{2|\tanh q|^2}\Big(1+|\tanh q|^2\Big)\Bigg\} \quad ;$$

$$J_{2,1} = A_{T_1} + UA_{X_1} \quad ; \quad J_{2,2} = \frac{3i\sigma^3A^2}{4\sinh^2 q}$$

where α defined by

$$\alpha \equiv e^{\psi-\psi^*} \tag{A 35}$$

is a coefficient which denotes the nonlinear forcing mechanism. Note that $\alpha = 1$ everywhere before the blocking point. Beyond the blocking point α will either be an exponentially growing or decaying function depending upon the choice of the wave number.
At $m = 0$ we have

$$\Phi_{2,0_{zz}} = 0 \qquad -h \le z \le \eta_c$$

$$\Phi_{2,0_z} = 0 \qquad z = -h$$

and thus get

$$\Phi_{2,0} = \Phi_{2,0}(X_1, X_2, Y_1, Y_2, T_1, T_2, \cdots) \tag{A 37}$$

At $m = 1$ we have

$$\Bigg(\frac{\partial^2}{\partial z^2} - k^2\Bigg)\Phi_{2,1} = -\frac{kA_{X_1}}{\sigma}\Big(\frac{\cosh Q}{\cosh q}\Big); \quad -h \le z \le \eta_c$$

$$\Phi_{2,1_z} = 0; \quad z = -h$$

$$\left(\frac{\partial}{\partial z} - \sigma^2\right)\Phi_{2,1} = A_{T_1} + UA_{X_1}; \quad z = \eta_c$$

Substituting the forcing terms $F_{2,1}, G_{2,1}$ and $J_{2,1}$, and solution at $n = 1$ in (A 28) yields

$$A_{T_1} + (U + C_g)A_{X_1} = 0 \tag{A 39}$$

where C_g is the group velocity for a wave propagating in a frame of reference with the current and is given by

$$C_g = \frac{\sigma}{2k}\left(1 + \frac{2q}{\sinh 2q}\right) \tag{A 40}$$

The homogeneous solution for $\Phi_{2,1}$ is the same as $\Phi_{1,1}$, and the particular solution can be obtained by the method of variation of parameters to yield

$$\Phi_{2,1} = -\frac{iB}{2\sigma}\left(\frac{\cosh Q}{\cosh q}\right) - \left(\frac{Q \sinh Q}{2k\sigma \cosh q}\right)A_{X_1}$$

The first term in the expression can be absorbed in the solution for $\Phi_{1,1}$ and we get

$$\Phi_{2,1} = -\left(\frac{Q \sinh Q}{2k\sigma \cosh q}\right)A_{X_1} \tag{A 41}$$

At $m = 2$ we have

$$\left(\frac{\partial^2}{\partial z^2} - 4k^2\right)\Phi_{2,2} = 0; \quad -h \le z \le \eta_c$$

$$\Phi_{2,2_z} = 0; \quad z = -h$$

$$\left(\frac{\partial}{\partial z} - 4\sigma^2\right)\Phi_{2,2} = \frac{3i\sigma^3 A^2}{4\sinh^2 q}; \quad z = \eta_c$$

which yields the particular solution

$$\Phi_{2,2} = -\frac{3i\sigma A^2 \cosh 2Q}{16 \sinh^4 q} \tag{A 43}$$

Eqns (A 37), (A 41) and (A 43) give the solution for Φ_2, and together with the solutions for Φ_1 and η_1 can be substituted in the forcing term for η_2 to yield at the different harmonics

$$\eta_{2,0} = -\left[\left(\Phi_{1,0_{T_1}} + U\Phi_{1,0_{X_1}}\right) + \frac{|A|^2}{4}\alpha\left(\frac{|\sigma|^2(1 + |\tanh q|^2)}{|\tanh q|^2} - (k \tanh q + c.c.)\right)\right] \tag{A 44a}$$

$$\eta_{2,1} = \frac{i}{2\sigma}\left[A_{T_1} + \left(U - \frac{q\sigma \tanh q}{k}\right)A_{X_1}\right] \tag{A 44b}$$

$$\eta_{2,2} = \frac{k \cosh q}{8 \sinh^3 q}(2\cosh^2 q + 1)A^2 \tag{A 44c}$$

A.2.3. *Third order solution*

To determine the governing envelope equations at third order we only need to evaluate the solvability condition at $n = 3$. Using the solutions at $n = 2$ and $n = 1$, the forcing terms for $m = 0, 1$ at third order are given by

$$F_{3,0} = -\Big(\Phi_{1,0_{X_1X_1}} + \Phi_{1,0_{Y_1Y_1}}\Big)$$

$$F_{3,1} = \frac{i}{2\sigma}\Big(A_{X_1X_1} + A_{Y_1Y_1}\Big)\frac{\cosh Q}{\cosh q} - \frac{1}{2}\left[k\Big(\frac{A\cosh Q}{\sigma\cosh q}\Big)_{X_2} + \Big(\frac{kA\cosh Q}{\sigma\cosh q}\Big)_{X_2}\right] \qquad \text{(A 45}a)$$
$$+ \frac{iQ\sinh Q}{\sigma\cosh q}A_{X_1X_1}$$

$$G_{3,0} = 0 \quad ; \quad G_{3,1} = -h_{X_2}\frac{kA}{2\sigma\cosh q} \qquad \text{(A 45}b)$$

$$J_{3,0} = -\Big(\Phi_{1,0_{T_1T_1}} + 2U\Phi_{1,0_{X_1T_1}} + U^2\Phi_{1,0_{X_1X_1}}\Big)$$
$$+ \frac{\alpha}{2}\left\{\Big(\frac{\sigma-\sigma^*}{|\sigma|^2}\Big)(A_{X_1}A^*R_1 - A^*_{X_1}AR_1^*) + \Big\{A_{X_1}A^*(\frac{R_2}{2} + R_3) + c.c.\Big\}\right\}$$
$$J_{3,1} = \frac{Ub_{X_2}}{b}Y_1A_{Y_1} + \frac{kA}{2\sigma}\eta_{cX_2} + \frac{A}{2b}(Ub)_{X_2} + i\Big(\frac{C_g^2}{2\sigma} + \frac{q\sigma^2C_g}{k^2}\Big)A_{X_1X_1} \qquad \text{(A 45}c)$$
$$+ \frac{1}{2}\Big(A_{T_2} + UA_{X_2}\Big) + \frac{A_{T_2}}{2} + \frac{U\sigma}{2}\Big(\frac{A}{\sigma}\Big)_{X_2}$$
$$- \frac{i\sigma kA}{\sinh 2q}\left(\Phi_{1,0_{T_1}} + \Big(U - \frac{\sinh 2q}{\sigma}\Big)\Phi_{1,0_{X_1}}\right) + i\alpha|A|^2A(R_4 + R_5)$$

where

$$R_1 = k^* + \frac{q|k|^2\sigma^2}{k^2} + (\sigma^*)^2(q + \tanh q) \qquad \text{(A 46}a)$$

$$R_2 = \frac{k}{\sigma}(2 - \tanh^2 q) - \frac{q\tanh q}{k}\Big(\frac{k^2}{\sigma\cosh^2 q}\Big)^* \qquad \text{(A 46}b)$$

$$R_3 = C_g\Big(\frac{|k|^2}{|\sigma|^2} - \frac{(k^*)^2}{2|\sigma|^2\cosh^2 q^*} - \sigma(\sigma - \sigma^*)\Big) \qquad \text{(A 46}c)$$

$$R_4 = \frac{(\sigma - \sigma^*)}{4|\sigma|^2}|k|^2(k + k^*)(\tanh q + \tanh q^*) \qquad \text{(A 46}d)$$

$$R_5 = \frac{1}{8\sinh^4 q}\left\{\frac{3|k|^2}{|\sigma|^2}\sigma^2(2\sigma - \sigma^*)\cosh 2q + 3k|\sigma|^2(2\sigma - \sigma^*)\sinh 2q\right.$$
$$+ 3\sigma k^2(1 - 2\sinh^2 q) - \sigma^3\sinh^2 q\Big(\frac{|\sigma|^2(1 + |\tanh q|^2)}{|\tanh q|^2}$$
$$- (k\tanh q + k^*\tanh q^*)\Big) - \frac{|k|^2\sigma^*\sinh 2q(1 + 2\cosh^2 q)}{2\sinh 2q^*} \qquad \text{(A 46}e)$$
$$- \sinh^2 q\Big(\frac{|k|^2\sigma^3}{|\sigma|^2} + \frac{k(k - k^*)}{\sigma}\sinh^2 q\Big(\frac{|k|^2}{|\sigma|^2} + |\sigma|^2\Big)\Big)$$
$$\left. + \frac{|k|^2}{|\sigma|^2}\sigma\sinh^4 q(k + k^*)(\tanh q + \tanh q^*)\right\}$$

Substituting the forcing terms in (A 26) and (A 28) and simplifying, we get a set of coupled equations

$$\Phi_{1,0_{T_1T_1}} + 2U\Phi_{1,0_{X_1T_1}} + U^2\Phi_{1,0_{X_1X_1}} - (h+\eta_c)\Big(\Phi_{1,0_{X_1X_1}} + \Phi_{1,0_{Y_1Y_1}}\Big)$$
$$= \frac{\alpha}{2}\left\{\Big(\frac{\sigma-\sigma^*}{|\sigma|^2}\Big)(A_{X_1}A^*R_1 - A^*_{X_1}AR_1^*) + \Big\{A_{X_1}A^*\big(\frac{R_2}{2}+R_3\big) + c.c.\Big\}\right\} \tag{A 47a}$$

$$2A_{T_2} + 2(U+C_g)A_{X_2} + \sigma\Big(\frac{U+C_g}{\sigma}\Big)_{X_2}A - i\sigma_{kk}A_{X_1X_1} - i\frac{C_g}{k}A_{Y_1Y_1}$$
$$+\frac{Ub_{X_2}}{b}Y_1A_{Y_1} - \frac{2i\sigma kA}{\sinh 2q}\left(\Phi_{1,0_{T_1}} + \Big(U - \frac{\sinh 2q}{\sigma}\Big)\Phi_{1,0_{X_1}}\right) \tag{A 47b}$$
$$+ 2i\alpha|A|^2A(R_5+R_6) = 0$$

where

$$\sigma_{kk} = \frac{2q\sigma\cosh^2 q}{k^2\sinh 2q} - \frac{C_g^2}{\sigma} - \frac{2q\sinh qC_g}{k\cosh q} \tag{A 48}$$

The variation in the channel width can be taken into account by integrating (A 47) across the channel and using the lateral boundary conditions. From (A 14) and (A 17) the lateral boundary conditions is given by

$$\Phi_{1,0_{Y_1}} = 0; \quad Y_1 = \pm\epsilon b \tag{A 49a}$$

$$A_{Y_1} = \pm i\epsilon kAb_{X_2}; \quad Y_1 = \pm\epsilon b \tag{A 49b}$$

Integrating (A 47) across $Y_1 = \pm\epsilon b$ and using (A 49) we get a set of coupled equations for the width averaged amplitude $\bar{A}$, and long wave $\bar{\Phi}_{1,0}$

$$\bar{\Phi}_{1,0_{T_1T_1}} + 2U\bar{\Phi}_{1,0_{X_1T_1}} + (U^2-(h+\eta_c))\bar{\Phi}_{1,0_{X_1X_1}}$$
$$= \frac{\alpha}{2}\left\{\Big(\frac{\sigma-\sigma^*}{|\sigma|^2}\Big)(\bar{A}_{X_1}\bar{A}^*R_1 - \bar{A}^*_{X_1}\bar{A}R_1{}^*) + \Big\{\bar{A}_{X_1}\bar{A}^*\big(\frac{R_2}{2}+R_3\big) + c.c.\Big\}\right\} \tag{A 50a}$$

$$2\bar{A}_{T_2} + 2(U+C_g)\bar{A}_{X_2} + \frac{\sigma}{b}\Big(\frac{(U+C_g)b}{\sigma}\Big)_{X_2}\bar{A} - i\sigma_{kk}\bar{A}_{X_1X_1}$$
$$-\frac{2i\sigma k\bar{A}}{\sinh 2q}\left(\bar{\Phi}_{1,0_{T_1}} + \Big(U-\frac{\sinh 2q}{\sigma}\Big)\bar{\Phi}_{1,0_{X_1}}\right) + 2i\alpha|\bar{A}|^2\bar{A}(R_4+R_5) = 0 \tag{A 50b}$$

Eqn. (A 50) is a third order weakly non-linear evolution model for a narrow-banded wave envelope propagating on a strong current in a narrow varying channel. The model is also valid beyond the blocking point.

For sake of convenience we shall rewrite (A 50) in dimensional form

$$\bar{\Phi}_{1,0_{tt}} + 2U\bar{\Phi}_{1,0_{xt}} + (U^2 - g(h+\eta_c))\bar{\Phi}_{1,0_{xx}}$$
$$= \frac{\alpha g^2}{2}\left\{\Big(\frac{\sigma-\sigma^*}{|\sigma|^2}\Big)(\bar{A}_x\bar{A}^*R_1 - \bar{A}^*_x\bar{A}R_1{}^*) + \Big\{\bar{A}_x\bar{A}^*\big(\frac{R_2}{2}+R_3\big) + c.c.\Big\}\right\} \tag{A 51a}$$

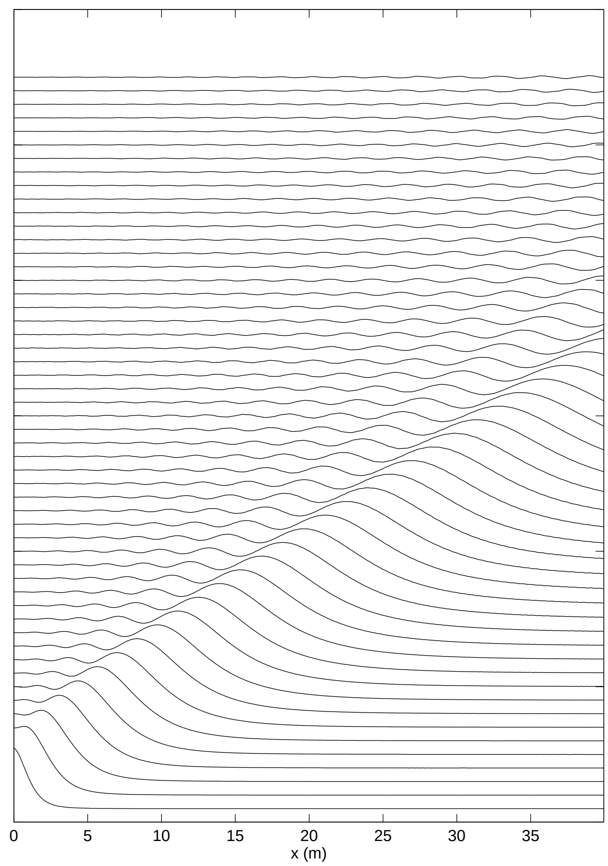

FIGURE 23. Snapshots of the spatial evolution of the wave envelope for a monochromatic wave in a uniform domain(T = 1.2s,U = 0). Vertical axis corresponds to the amplitude envelope in m.

$$
\begin{aligned}
&2\bar{A}_t + 2(U + C_g)\bar{A}_x + \frac{\sigma}{b}\left(\frac{(U + C_g)b}{\sigma}\right)_x \bar{A} - i\sigma_{kk}\bar{A}_{xx} \\
&- \frac{2i\sigma k\bar{A}}{g\sinh 2q}\left(\bar{\Phi}_{1,0_t} + \left(U - \frac{g\sinh 2q}{\sigma}\right)\bar{\Phi}_{1,0_x}\right) + 2i\alpha|\bar{A}|^2\bar{A}(gR_4 + R_5) = 0
\end{aligned}
\tag{A 51b}
$$

where the primes have been omitted for brevity. The expression for σ is now given by

$$
\sigma^2 = gk \tanh q \tag{A 52}
$$

The expressions for the coefficients R_1 to R_5, C_g and σ_{kk} remain unchanged except that they are now evaluated with the dimensional values of σ and k.

Appendix B. Numerical filter

In Section 3.1 we found that the simplified version of the evolution equation (eqn. (3.7)) yields two roots for a plane wave, of which (3.9a) is the correct root. There are several examples in the literature of numerical simulations of monochromatic wave envelopes in a uniform medium showing that the models pick up the correct root (see Mei (1992)). Similar results have also been obtained in our numerical model for a monochromatic wave (see Figure 23).

However, a varying channel leads to the development of instabilities which propagate backwards. To illustrate this point consider the linearized version of (3.3)

$$2\bar{A}_t + 2(U + C_g)\bar{A}_x + \frac{\sigma}{b}\Big(\frac{(U + C_g)b}{\sigma}\Big)_x \bar{A} - i\sigma_{kk}\bar{A}_{xx} = 0 \tag{B 1}$$

Once again assuming a plane wave solution for the wave amplitude

$$\bar{A} = ae^{i(Kx - \Omega t)}$$

and substituting in the equation we get

$$\Omega = (U + C_g)K + K^2\frac{\sigma_{kk}}{2} - i\frac{\gamma_s}{2} \tag{B 2}$$

where

$$\gamma_s = \frac{\sigma}{b}\Big(\frac{(U + C_g)b}{\sigma}\Big)_x$$

or

$$\Omega = \Omega_r - i\frac{\gamma_s}{2}$$

and

$$A = a_0 e^{-\frac{\gamma_s}{2}} e^{i(Kx - \Omega_r t)} \tag{B 3}$$

For a channel which contracts in the direction of wave propagation, $\gamma_s < 0$ and according to (B 3) this would lead to the growth of instabilities. In a domain that is very slowly varying the growth of these instabilities may be insignificant. However in our experimental tests the domain varies abruptly over a few wave lengths (see Figure 1) and the instabilities are expected to grow faster.

Numerical tests have thus been conducted to study the growth of instabilities in the varying domain. The numerical domain used is similar to the one used in the experiments, except that the constricting channel is described by a continuous function to remove discontinuities. The domain width was defined as

$$b(x) = 0.48 - 0.12\tanh(2(x - x_0)) \tag{B 4}$$

where x_0 is defined as the mid point of the transition region, and for our simulations $x_0 = -1.4$ m. For the simulations $\Delta x = 0.05$ m, $\Delta t = 0.0074$ s, $h = 0.5$ m and initial amplitude $A_0 = 0.01$m. Flow is prescribed through a discharge Q, and velocity profile determined using a simple continuity equation

$$U(x) = \frac{Q}{b(x)h}$$

For the case with no opposing current ($Q = 0$) Figure 24 shows the spatial snapshots of the wave envelope at different times. The limits of the region where the channel is narrowing is shown by the dashed line. The growth of the instability in the constricting part of the channel can be clearly observed. This instability propagates along the spurious root K_2, and since this root has a negative group velocity the disturbance is propagated backward into the domain. Introducing an opposing current ($Q = -0.05$ m^3/s) leads to a larger value of γ_s and consequently a faster growth of the instability as can be seen in Figure 25.

Considering now a test case in which the numerical domain consists of an expanding channel instead of a contracting channel,

$$b(x) = 0.48 + 0.12\tanh(2(x - x_0)) \tag{B 5}$$

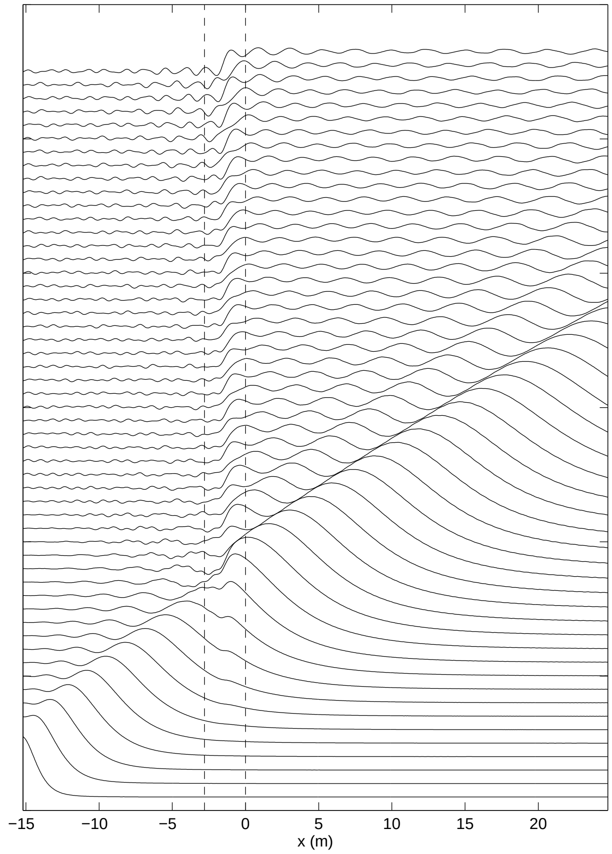

FIGURE 24. Snapshots of the spatial evolution of the wave envelope for a monochromatic wave in a contracting channel. Spatial location of the start and end of narrowing channel denoted by dashed line. (T = 1.2s,Q = 0)

and using the same initial conditions that were used in Figure 25 we observe that the instability is now damped out as $\gamma_s > 0$ (see Figure 26).

To validate model with experimental tests conducted on narrow-banded waves our numerical domain has to have a contracting channel. We thus need a numerical filter which will damp out the instability that propagates along the root K_2. A '3 point' filter is used for this purpose (Shapiro 1970).

$$A_{new}|_{x=j\Delta x} = \gamma_f A|_{x=j\Delta x} + \frac{1-\gamma_f}{2}\Big(A|_{x=(j-1)\Delta x} + A|_{x=(j+1)\Delta x}\Big) \tag{B 6}$$

Substituting

$$A = A_0 e^{i(Kx-\Omega t)}$$

in the above equation, we get an amplification factor or response function R as a function of K and Δx

$$R = \frac{A_{new}}{A} = \gamma_f + (1-\gamma_f)\cos(K\Delta x) \tag{B 7}$$

where γ_f is a weighting function. Damping occurs when $R < 1$. Substituting (3.10) in (B 7) we can get the response functions for the two roots K_1 and K_2 (see Figure 27).

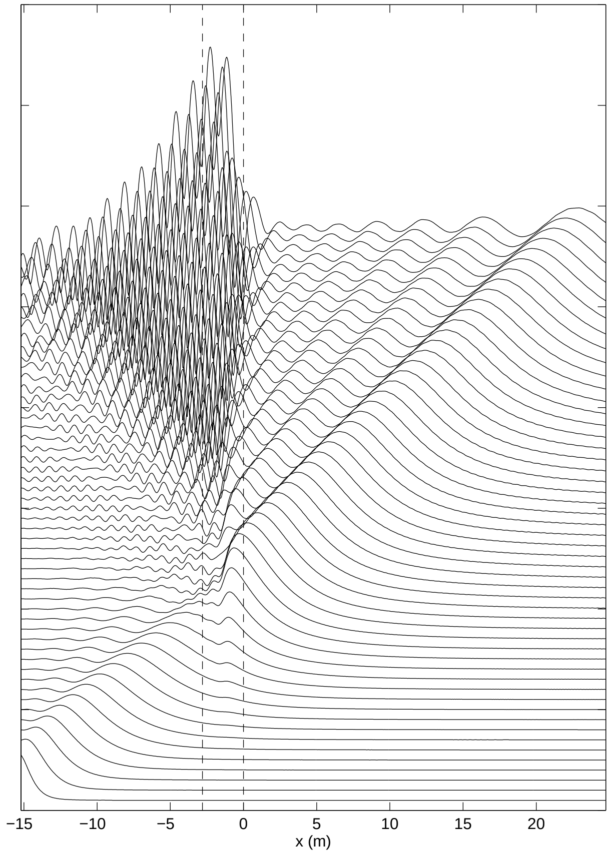

FIGURE 25. Snapshots of the spatial evolution of the wave envelope for a monochromatic wave in a contracting channel. Spatial location of the start and end of contracting channel denoted by dashed line. (T = 1.2s,Q = -0.05 m^3/s)

The undesired root K_2 has a much higher damping rate, and can be damped out. Figure 28 shows the snapshots of the evolution of the same monochromatic wave as shown in Figure 25 with the exception that a 3 point filter with $\gamma_f = 0.65$ is used every 10 time steps. The filter damps out the backward propagating instability, with negligible effects on the forward propagating envelope.

REFERENCES

Bretherton, F. P. and Garrett, C. J. R. (1969). Wavetrains in inhomogeneous moving media. *Proc. Roy. Soc. London A.*, **302**, 529–554.

Chawla, A. and Kirby, J. T. (1998). Experimental study of wave breaking and blocking on opposing currents. In *Proc.* 26th *Int. Conf. Coastal Engineering*, 759–772, Copenhagen. ASCE.

Chawla, A. and Kirby, J. T. (1999). Waves on opposing currents: Data report. Technical Report CACR-99-03, Center for Applied Coastal Research, University of Delaware.

Chawla, A. and Kirby, J. T. (2002). Monochromatic and random wave breaking at blocking points. *J. Geophys. Res.*, **107(C7)**, 10.1029/2001JC001042.

Chen, Q., Madsen, P. A., Schäffer, H. A., and Basco, D. R. (1998). Wave-current interaction based on an enhanced Boussinesq approach. *Coastal Eng.*, **33**, 11–39.

Davey, A. (1972). The propagation of a weak non-linear wave. *J. Fluid Mech.*, **53**, 769–781.

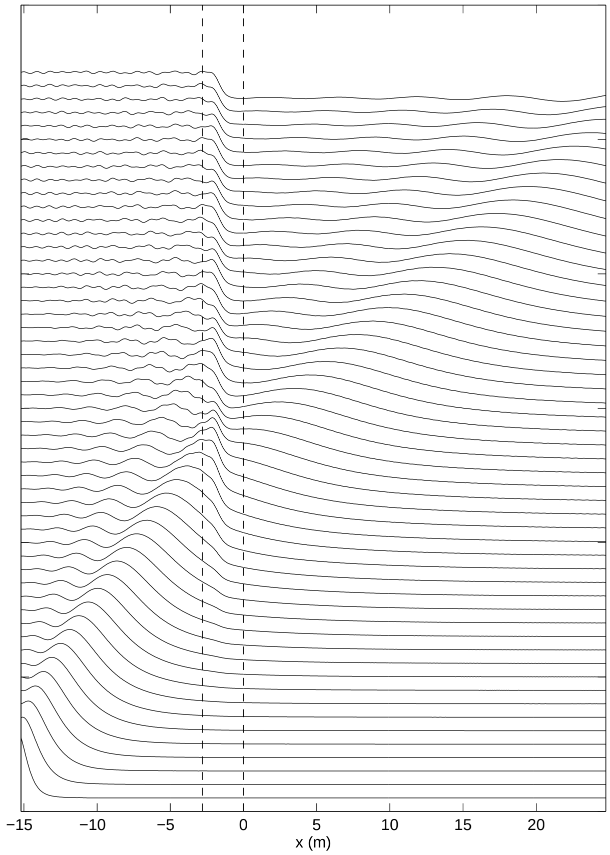

FIGURE 26. Snapshots of the spatial evolution of the wave envelope for a monochromatic wave in an expanding channel. Spatial location of the start and end of expanding channel denoted by dashed line. (T = 1.2s,Q = -0.05 m^3/s)

Gerber, M. (1987). The Benjamin-Feir instability of a deep water Stokes wave packet in the presence of a non-uniform medium. *J. Fluid Mech.*, **176**, 311–332.

Hasimoto, H. and Ono, H. (1972). Non-linear modulation of gravity waves. *J. Phys. Soc. Jpn.*, **33**, 805–811.

Jonsson, I. G. (1990). Wave-current interactions. In *The Sea*, volume 9, pages 65–120. Wiley Interscience, New York.

Lai, R. J., Long, S. R., and Huang, N. E. (1989). Laboratory studies of wave-current interaction:kinematics of the strong interaction. *J. Geophys. Res.*, **94**, 16201–16214.

Lin, R. Q. and Perrie, W. (1997). A new coastal model. part iii: Nonlinear wave-wave interaction. *J. Phys. Ocean.*, **27**, 1813–1826.

Longuet-Higgins, M. and Stewart, R. (1960). Changes in the form of short gravity waves on long waves and tidal currents. *J. Fluid Mechanics*, **8**, 565–583.

Mei, C. C. (1992). *The Applied Dynamics of Ocean Surface Waves*. World Scientific, second edition.

Moreira, R. and Peregrine, D. (2001). Interactions between water waves and singularities. In *Proc. IUTAM Symp. on free surface flows*, pages 205–212, Birmingham.

Moreira, R. M. (2001). *Non-linear interactions between water waves, free surface flows and singularities*. Ph.D. thesis, University of Bristol, UK.

Peregrine, D. H. (1976). Interaction of water waves and currents. *Advances in Applied Mechanics*, **16**, 9–117.

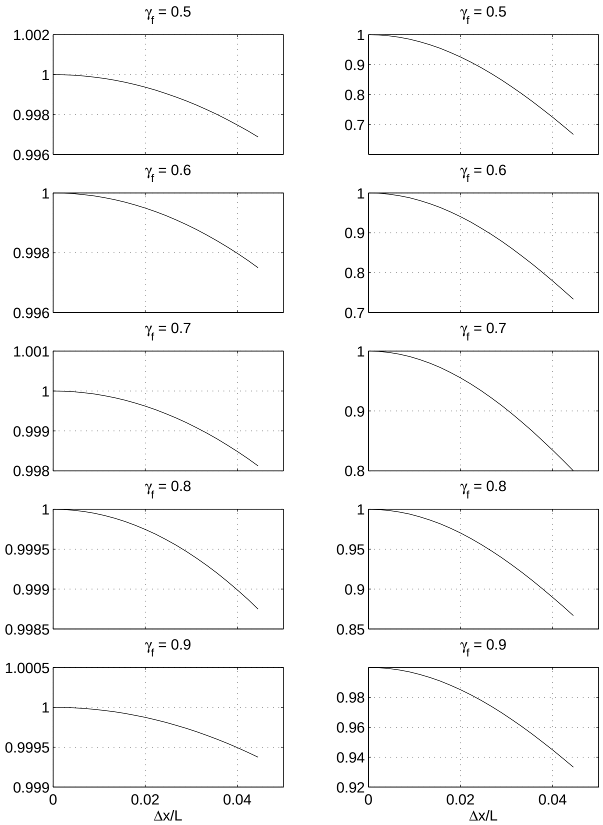

FIGURE 27. Response function for a 3 point filter. Left panels correspond to K_1; Right panels correspond to K_2 (T = 1.2 s; $\dfrac{\Omega}{\sigma} = 0.2$)

Peregrine, D. H. and Smith, R. (1979). Nonlinear effects upon waves near caustics. *Phil. Trans. Roy. Soc.*, **292(A)**, 341–370.

Shapiro, R. (1970). Smoothing, filtering and boundary effects. *Rev. Geophys. and Space Phys.*, **8**, 359–387.

Shyu, J. H. and Phillips, O. M. (1990). The blockage of gravity and capillary waves by longer waves and currents. *J. Fluid Mech.*, **217**, 115–141.

Smith, R. (1975). Reflection of short gravity waves on a non-uniform current. *Math. Proc. Camb. Phil. Soc.*, **78**, 517–525.

Stiassnie, M. and Dagan, G. (1979). Partial reflexion of water waves by non-uniform adverse currents. *J. Fluid Mech.*, **92**, 119–129.

Suastika, I. K., Jong, M., and Battjes, J. (2000). Experimental study of wave blocking. In *Proc. 27^{th} Int. Conf. Coastal Engineering.*, volume 1, pages 223–240, Sydney. ASCE.

Thomas, G. P. and Klopman, G. (1997). Wave-current interactions in the nearshore region. In J. N. Hunt, editor, *Gravity waves in water of finite depth*. 255−319. Computational Mechanics Publications, Boston.

Trulsen, K. and Mei, C. C. (1993). Double reflection of capillary/gravity waves by a non-uniform current: a boundary-layer theory. *J. Fluid Mech.*, **251**, 239–271.

Turpin, F. M., Benmoussa, C., and Mei, C. C. (1983). Effects of slowly varying depth and current on the evolution of a Stokes wavepacket. *J. Fluid Mech.*, **132**, 1–23.

Yuen, H. C. and Lake, B. M. (1975). Nonlinear deep water waves: Theory and experiment. *Phys. Fluids*, **18**, 956–960.

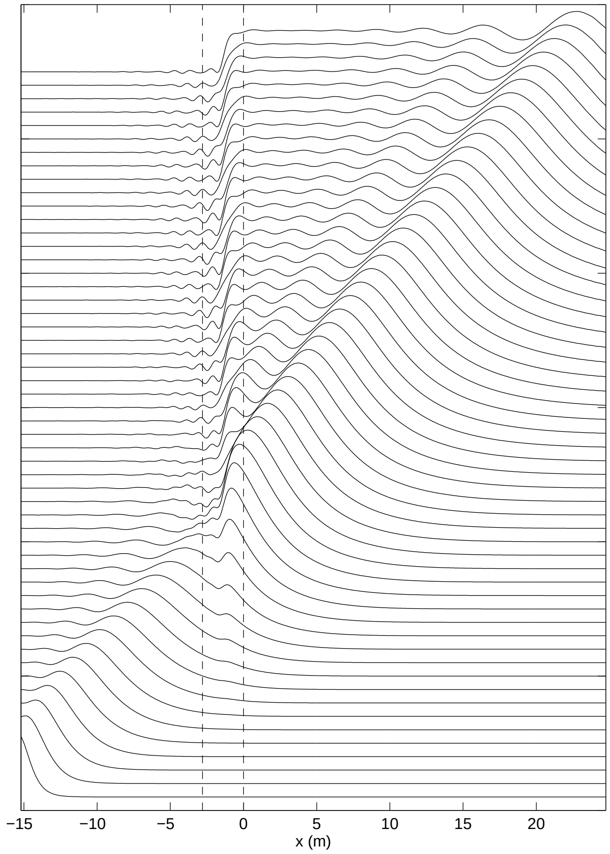

FIGURE 28. Snapshots of the spatial evolution of the wave envelope for a monochromatic wave for the same conditions as in Figure 25, but now using a 3 point filter (T = 1.2s,γ_f = 0.65)

Zakharov, V. E. (1968). Stability of periodic waves of finite amplitude on the surface of a deep fluid. *J. Applied Mech. Phys.*, **9**, 190–194.

Zakharov, V. E. and Shabat, A. B. (1972). Exact theory of two-dimensional self-focusing and one-dimensional self-modulating waves in non-linear media. *Sov. Phys. – JETP*, **34**, 62–69.